ELECTROCHEMICAL AND OPTICAL CHARACTERIZATION OF ELECTROCHROMIC TUNGSTEN OXIDE SYNTHESIZED BY PECVD

by

Michael Seman

ProQuest LLC.
789 East Eisenhower Parkway
P.O. Box 1346
Ann Arbor, MI 48106 – 1346

A thesis submitted to the Faculty and the Board of Trustees of the Colorado School of Mines in partial fulfillment of the requirements for the degree of *Master of Science* (Chemical Engineering).

Golden, Colorado

Date 4/8/04

Signed: _____
Michael Seman

Approved: _____
Dr. Colin Wolden
Thesis Advisor

Golden, Colorado

Date 4/8/04

_____
Dr. James Ely
Professor and Head
Department of
Chemical Engineering

ABSTRACT

Electrochromic materials have the unique ability to reversibly alter their optical state from clear to opaque in response to an applied voltage. These materials have long been of interest for a variety of applications, including smart windows, variable reflectance mirrors, displays, and gasochromatic sensors. In particular, large-scale deployment of smart windows could have a significant impact on national energy expenditures. It has been estimated that electrochromic windows have the potential of reducing annual U.S. energy consumption by several quadrillion (10^{15}) Btus, or quads. Tungsten oxide is the electrochromic material of choice for smart windows.

This thesis presents the development of plasma-enhanced chemical vapor deposition (PECVD) as a technique to form electrochromic tungsten oxide thin films from gas mixtures of WF_6, O_2, and H_2. The chemistry of this system was investigated using optical emission spectroscopy (OES). The plasma composition and deposition rate were examined as a function of operating conditions. Growth rates were maximized when the atomic fluorine density was attenuated and the atomic oxygen density was saturated. With the exception of hydrogen scavenging of fluorine radicals, the major reaction pathway was simply dissociation, as the densities of the atomic species were proportional to the initial reagent composition. An apparatus was built to evaluate electrochemical performance in direct registry with optical transmission. Of the many plasma parameters it was found that ion bombardment has the most dramatic impact on electrochromic performance. Ion bombardment was found to increase film density, as inferred from

measurements of the refractive index. Efficient hydrogen intercalation was observed only in those films whose refractive index at 400 nm were less than 2.1.

A quantitative evaluation of PECVD WO_3 was carried out through chronoamperometry in concert with optical transmission to determine diffusion and absorption coefficients using both H^+ and Li^+ containing electrolytes. The absorption coefficients were similar for both ions, scaling with the degree of intercalation to 50,000 cm^{-1} in the opaque state. The diffusion coefficients for optimized films were found to be relatively insensitive to the degree of ion intercalation, with values of $\sim 10^{-9}$ and $\sim 10^{-10}$ cm^2/s for H^+ and Li^+, respectively. These values are about an order of magnitude greater than values reported for vacuum-deposited films, which was attributed to the low relative density of the PECVD films. The diffusion and absorption coefficients were incorporated into a model that successfully reproduced transient optical performance.

A long-term goal of our group is to deposit a complete electrochromic device through PECVD. Previous projects have examined the formation of transparent conducting oxide contacts. A complete device also requires an electrolyte and an ion storage layer. A detailed literature review was performed to identify candidate oxides for PECVD synthesis. Tantalum oxide was identified as top electrolyte, while either nickel or vanadium oxide could serve as the ion storage layer. It is recommended that the next step towards a complete device be the optimization of a vanadium oxide ion storage layer. Synthesis and characterization are similar to WO_3, and the two could be readily combined with an organic electrolyte to form a complete device.

TABLE OF CONTENTS

LIST OF FIGURES

LIST OF TABLES

ACKNOWLEDGEMENTS

I would like to take this time to recognize the people who helped me complete this work. First I would like to thank my advisor Dr. Colin Wolden for his guidance and help throughout this project. Also I would like to acknowledge Dr. Joshua Robbins, a former student who recently completed his doctorate and whose previous work in the lab prepared the way for my work. In addition, Jackie Leaf, Cassandra Fry, and John Harvey all contributed many hours of their time to this project.

This work was supported in part by the National Science Foundation through Career Grant No. CTS-0093611.

CHAPTER 1

INTRODUCTION

Since Satyen K. Deb first discovered the electrochromic properties of tungsten oxide in 1973[1], there has been sustained research to convert this phenomenon from a laboratory novelty to practical devices. Electrochromic materials have the unique ability to reversibly alter their optical state from clear to opaque in response to an applied voltage. An electrochromic film is reversibly colored through the intercalation of a light ion (M^+), typically H^+ or Li^+, in response to a small externally applied electric field. Electrochromic materials may exhibit an optical response upon ion insertion, cathodic coloration, or upon ion extraction, anodic coloration. Examples of these reactions can be summarized as follows:

Cathodic coloration:

$$\underset{\text{(Clear)}}{WO_3} + xe^- + xM^+ \leftrightarrow \underset{\text{(Opaque)}}{M_xWO_3} \qquad (1.1a)$$

Anodic coloration:

$$\underset{\text{(Opaque)}}{NiO} + xe^- + xM^+ \leftrightarrow \underset{\text{(Clear)}}{M_xNiO} \qquad (1.1b)$$

where x is commonly referred to as the degree or extent of intercalation. The intercalation level dictates the degree of transmission change and is a key parameter in evaluation of

electrochromic films. Figure 1.1 summarizes the many transition metal elements whose oxides have been found to possess electrochromic behavior.

The absorption mechanism of tungsten oxide is generally accepted to be a result of a small polaron absorption. In cathodic coloration of tungsten oxide, injected electrons cause an increase in the number of W^{+5} sites. Schrimer et al.[2] proposed that the optical absorption is caused by the small polaron transitions between two nonequivalent, neighboring sites of tungsten, W^{+5} and W^{+6}.

$$h\nu + W^{+5}(A) + W^{+6}(B) \rightarrow W^{+5}(B) + W^{+6}(A) \qquad (1.2)$$

where A and B are neighboring atoms. According to Equation 1.2, inserted electrons are localized in W^{+5} sites and polarize the surrounding lattice to form small polarons. Incident photons are absorbed by these small polarons which hop from one site to another[3]. Others have argued that the transition occurs between W^{+4} and W^{+5} sites.

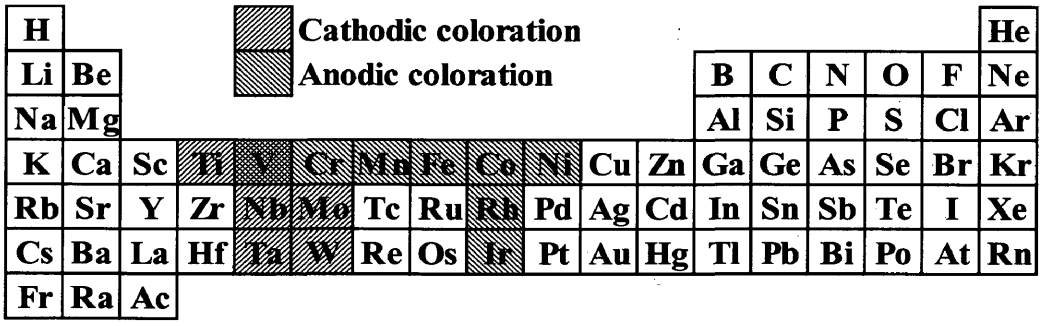

Figure 1.1: Summary of transition metals that form oxides displaying either cathodic or anodic coloration

Electrochromic materials are of interest in a variety of applications, including smart windows, variable reflectance mirrors, displays, and gasochromatic sensors. Figure 1.2 summarizes these applications[4]. Particular interest has been given to the development of smart windows (1.2a). Windows are the major source of energy loss in buildings. Smart windows allow building designers to modulate incoming solar radiation to drastically reduce heating and cooling costs. Large-scale deployment of such windows could have a huge impact on national energy expenditures. It has been estimated that electrochromic windows have the potential of reducing annual U.S. energy consumption by several quadrillion (10^{15}) Btus, or quads. The United States currently consumes a total of approximately 94 quads of energy per year[5]. There is also a developing niche market for specialty windows for architectural design. Additional motivation for development has come from the automotive industry for applications in glare control of truck and automobile mirrors (1.2b). Incorporation of pigments and patterning of electrochromic materials can serve for information displays, which may hold promise for applications in certain signs and labels (1.2c). Finally, the unique optical response of electrochromic materials may be incorporated as a sensor whose response is non-reactive in the presence of a volatile gas, particularly hydrogen (1.2d).

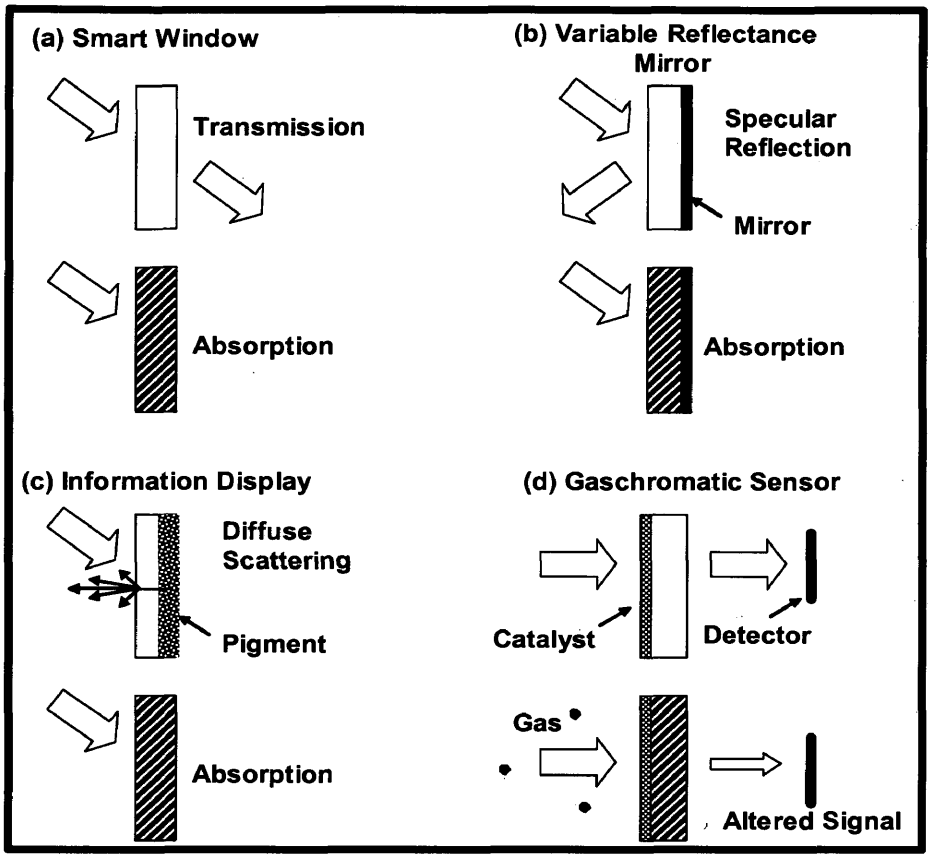

Figure 1.2: Four outlined principles for electrochromic material applications.

Typically electrochromic materials are deposited using physical vapor deposition (PVD) techniques such as sputtering, evaporation, or laser ablation. Chemical routes such as sol-gel techniques and chemical vapor deposition (CVD) have also been employed. In this thesis I will present the development of plasma enhanced chemical vapor (PECVD) deposition as an alternative approach to the synthesis of high quality WO_3. This chapter includes an overview of the specifics behind electrochromic device operation, a summary

of other important properties for electrochromic films, and a comparison between commonly employed deposition techniques and PECVD.

1.1 Electrochromic Device Basics: Operation and Evaluation

In general, an electrochromic device is a multi-layered structure consisting of four principal components, (i) an electrochromic layer, (ii) an ion storage layer, (iii) an ion conducting electrolyte (iv) and transparent conducting oxide (TCOs e.g. SnO_2 or In doped SnO_2, ITO) electrical contacts. Figure 1.3 shows a schematic of a typical device. In cathodic coloration, when a small voltage is applied across the electrodes, an ion is pulled from the storage layer, transported across the electrolyte, and combines with an electron in the electrochromic layer to cause the device to darken. Tungsten oxide is the leading electrochromic material. However other transition metal oxides have been shown to have similar properties[6]. Leading candidates for the ion storage layer include, nickel oxide, vanadium oxide, and mixed ceria containing oxides, in particular Ti-Ce oxide[7] and Zr-Ce oxide[8]. Both polymeric and solid state materials have been used for the electrolyte. Ta_2O_5 has been used as a solid-state electrolyte, while many polymers containing Li perchlorate or Li triflate are used in Li based devices. In polymer based devices, it is not enough to have ion conductivity, but good adhesion to both the electrochromic layer and the storage layer are necessary to avoid delamination and achieve sufficient device lifetime[4]. To achieve maximum change in transmission it is essential that the ion storage layer be

transparent upon ion insertion, or ideally exhibit the inverse behavior of the electrochromic layer. High quality conductive and transparent TCOs are also essential for optimum device performance.

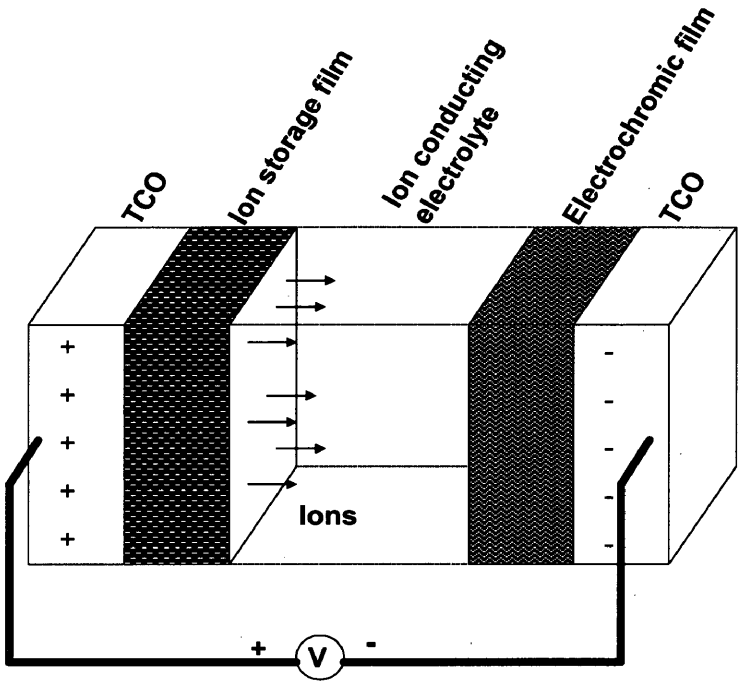

Figure 1.3: Basic components of an electrochromic device.

Three key device parameters are typically considered in the development of smart windows. First, the contrast ratio of clear state transmission to opaque state transmission should be greater than 4. Second, to justify the capital expenditure the device must demonstrate a lifetime of greater than 50,000 cycles. Finally, the switching time between bleached and opaque states should be minimized. This factor is most important in

information display and variable reflectance mirror applications. Table 1.1 summarizes additional important criteria for a complete electrochromic device from a published review article[9].

Performance parameter	Desired requirement
Clear state transmisson	60 to 80%
Colored state transmission	5 to 20%
Contrast ratio	4:1 to 10:1
Switching time (>0.1m2)	1 to 5 min
Cycle lifetime	> 50,000 cycles
Static lifetime	10 to 40 years
Darkened state memory	minutes to hours
Color	Neutral gray
Operating temperature	-20 to 85°C

Table 1.1: Desired performance criteria for electrochromic window.

1.2 Deposition of WO_3 from the Literature

Deposition of WO_3 is commonly performed through a variety of physical vapor deposition (PVD) techniques including plasma sputtering, thermal evaporation, and laser ablation. These techniques are similar in that particles are ejected from a metal or ceramic target and onto the substrate. Differences arise from the manner in which energy is supplied to volatize the target. In sputtering, a plasma is created by applying a voltage across a cathode and anode in the presence of a low pressure gas. The target is placed on

the cathode and the substrate on the anode. The plasma produces ions that are accelerated through the plasma sheath to collide and sputter the source material from the target. In reactive sputtering, the source consists of a tungsten target. Tungsten oxide is then deposited by sputtering the elemental tungsten in the presence of an oxygen/argon plasma. The argon to oxygen ratio plays a crucial role in controlling deposition rates and film properties. Tungsten oxide targets may also be cast and sputtered in either a pure argon plasma or argon/oxygen plasma. However, because ceramic targets are insulating, an rf discharge is required to prevent charge buildup on the targets. In contrast, reactive sputtering typically uses a DC discharge, which is typically cheaper and yields higher growth rates.

The simplest PVD technique is thermal evaporation, in which WO_3 powders are evaporated from a resistively heated refractory boat. However this offers limited control over the resulting film. More advanced evaporation techniques include e-beam and laser ablation. In both cases a high power laser or electron beam is used to vaporize WO_3 targets or W targets in the presence of oxygen. On the laboratory scale these techniques produce high quality, highly oriented films. However, neither deposition technique is viewed as an economic choice for electrochromic window manufacturing due to its cost and impracticality for large-scale production. Furthermore, the best performing films of WO_3 for smart window applications have been shown to be highly disordered, amorphous material.

Chemical based routes such as CVD and sol-gel techniques have also been employed for the deposition of tungsten oxide. Traditional thermal CVD uses temperatures of excess of 200°C to initiate and sustain decomposition and surface reactions of precursor gases[10,11]. In sol-gel techniques a solution of tungsten containing salts are spun cast onto a substrate and then oxidized by annealing in air[12]. Finally, electrodeposited films of WO_3 from a solution of a tungsten salts suspended in various organic alcohols have produced highly porous films with the best ion intercalation efficiency[13]. However, large area uniformity and time dependent deposition rates are problematic issues associated with this process.

1.3 Plasma CVD Background

The main advantage of PECVD is the ability to achieve the high deposition rates of thermal CVD at room temperature. PECVD has established itself as the technique of choice for low temperature deposition in the semiconductor industry and is routinely used to synthesize thin films including amorphous silicon, silicon dioxide, silicon nitride, and a variety of polymers. Where traditional CVD relies on thermal activation for dissociation of reactants, PECVD is initiated by high energy electrons. In addition, PECVD provides many parameters, such as pressure, power, and geometry that may be adjusted to tune film properties.

A capacitively coupled plasma such as the one used in this work, is created by flowing a low pressure gas through a high strength rf electric field. The plasma is composed of electrons, ions, and a variety of neutral atoms, molecules, and radicals. In the plasma, electrons are readily accelerated by the electric field and reach electron temperatures (T_e) of ~2-5 eV (15000-39000K). These high energy electrons are energetically equivalent to 50-125 kcal/mol, which is more than sufficient to dissociate most feed gases. However, the vast majority of the remaining ions and neutral species remain close to room temperature due to the inelastic nature of these collisons. Since T_e is so much greater than substrate or gas temperature, deposition temperatures are dramatically reduced.

In addition to high rates at low temperature, another advantage to PECVD is its versatility. PECVD allows one to tailor film properties for different applications. However, the flexibility that results from many adjustable parameters can also be a burden without proper insight. In this work we use optical emission spectroscopy (OES) to quantify plasma composition as a function of operating conditions. In particular, ion bombardment is one characteristic of a plasma processes that can greatly modify film composition, structure, and other properties. In our asymmetric configuration the degree of ion bombardment is controlled by choice of electrode and plasma power. The ion density, and thus the flux of ions is directly proportional to the rf power. In our system the grounded electrode is ~2 times larger than the powered electrode. In a plasma the flux of electrons to any surface is equal due to their high velocities. In order to maintain

charge neutrality the ion flux at all surfaces must also be equal. Power dissipation at the electrodes is primarily a result of ion bombardment, which is a product of the ion flux and sheath voltage. To accommodate this energy balance the sheath voltage at the smaller powered electrode is greater. In our configuration, the ions bombarding the powered electrode have ~6 times the energy of the ions hitting the grounded electrode[14].

In general, PECVD is a favorable deposition technique because of its high deposition rates at low temperature. With a wide range of operating parameters such as pressure, power, substrate temperature, and precursor flow rates PECVD is also useful as a versatile technique capable of depositing a wide range of film characteristics.

1.4 PECVD of WO_3

Despite the aforementioned advantages, PECVD has received relatively little attention as a viable deposition technique for WO_3. PECVD of WO_3 typically employs mixtures of the three reactants WF_6, O_2, and H_2. Tungsten hexafluoride decomposes readily in a plasma, however the reaction is reversible as the released fluorine radicals etch the film. To mitigate this issue hydrogen is added to scavenge atomic fluorine, forming HF. The global reaction may be expressed simply as

$$WF_6 + \text{Excess } O_2 + \text{Excess } H_2 \rightarrow WO_3 + HF + (H_2, O_2, H_2O) \qquad (1.3)$$

Tracy and Bensen[15] were the first to report on PECVD of WO_3 using these gases in a barrel reactor. They also used the solid metal carbonyl precursor $W(CO)_6$. This precursor eliminates concern due to fluorine, however it is much more difficult to handle and

control. Henley and Sacks[16] followed by focusing on the role of reactant composition, showing that both the H_2:WF_6 and the O_2:WF_6 ratios must be greater than unity in order to achieve high rates and quality films. However, the details of the plasma chemistry are highly complex, and kinetics remain largely unknown. In addition, there has been little quantitative evaluation of the electrochromic properties of PECVD WO_3.

Synthesis of metal oxides by PECVD has been a long-term goal of our research group. Previous work focused on PECVD synthesis of tin and zinc oxide that could be used as transparent electrodes[17-19]. The focus of this work is deposition of WO_3, but in principle a complete solid oxide electrochromic device could be fabricated by PECVD. This would further expand the benefits of using PECVD for smart window production. The entire process could be economically streamlined by employing a manufacturing line that efficiently deposits an entire device through in-line modulation of precursor gases.

The goal of this thesis is to understand the PECVD synthesis of WO_3 and evaluate the electrochromic response of this material as a function of operating conditions. Chapter 2 describes the specific experimental set-ups that were used for both deposition and analysis of WO_3 thin films. Chapter 3 provides a comprehensive study of the effects of operating conditions on the plasma composition and growth rate. It also provides a preliminary evaluation of the effects of plasma conditions on film performance. This greatly extends the work of the basic guidelines presented by Henley and Sacks[16]. Chapter 4 describes a quantitative evaluation of electrochemical and optical performance. To the best of our knowledge, Chapter 4 presents the first comprehensive analysis of ion

diffusion and optical performance for PECVD WO_3. The diffusion and absorption coefficients of both H^+ and Li^+ are reported as a function of intercalation. These values were incorporated into a numerical model that successfully predicts the transient optical response of these films. Finally, Chapter 5 presents a critical review of PECVD opportunities to fabricate the electrolyte and ion storage layers, along with recommendations for future work.

CHAPTER 2

EXPERIMENTAL DESIGN, THEORY, AND PRACTICE

2.1 PECVD Reactor Description and Operating Procedures

The reactor for this work was a custom-made, stainless steel thin film deposition system. A schematic of the entire system is given in Figure 2.1. The reactor was initially provided through an agreement with Green Development L.L.C. of Golden, CO, where it was employed for the deposition of high-quality amorphous silicon films. In our group's previous work, it was converted for PECVD of transparent conducting tin oxide and is described in a previous thesis[20]. This work utilizes essentially the same reactor with very few modifications, the only significant alteration was changing of the metal precursors to gaseous WF_6. Industrial grade Ar, O_2, and H_2 stored in gas cylinders were used. A small lecture cylinder of 99.9% WF_6 was purchased from Cerac Incorporated. Gas flow rates were controlled by UNIT electronic mass flow controllers (MFCs). All depositions were run at room temperature. The reactor pressure was controlled by an automated butterfly valve located in the exhaust line.

A detailed diagram of the deposition chamber is shown in Figure 2.2. The chamber was placed on a platform in the center of the large outer shell. Teflon rings were placed on the platform for spacers, and T-top screws were used to firmly attach the

chamber to the platform. These screws also serve to ground the chamber through the inlet gas piping.

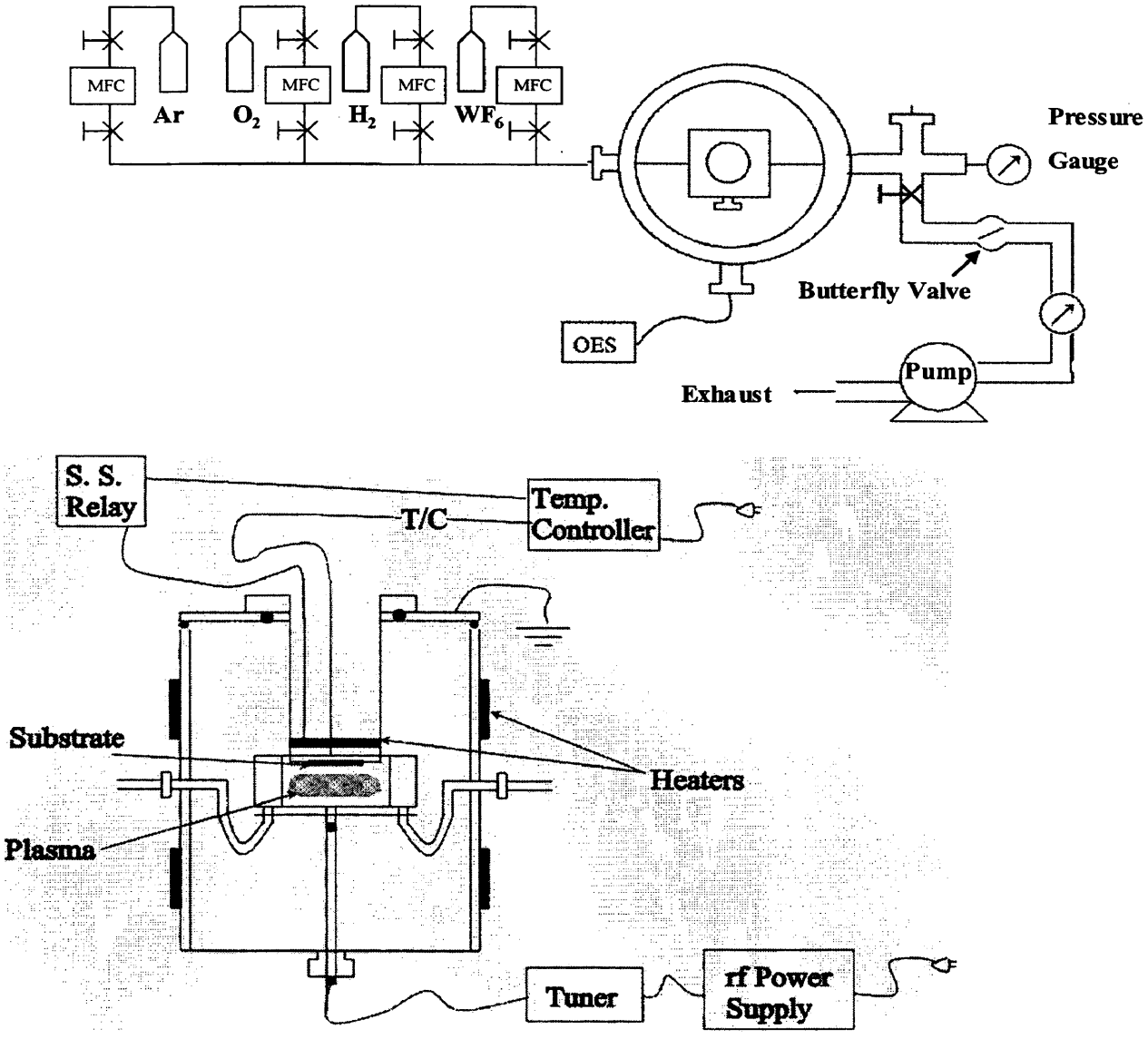

Figure 2.1: Schematic of the reactor. Top drawing depicts the top view, lower drawing is a cross-section of the inner and outer chamber.

As shown in Figure 2.2, the powered (lower) electrode is 5" square, and the rest of the chamber was grounded. The gap between the two electrodes was fixed at 1". Process gases flowed into the deposition chamber from the left-hand side and were distributed through seven evenly spaced 1 mm holes across the inlet side. Gases flow across the substrate and are exhausted on the right-hand side using a similar hole spacing with 0.25" holes connected to a flexible tube which opened to the exhaust line. Power was supplied by a 300 Watt power supply operating at 13.56 MHz.

Silicon wafers and transparent conducting tin oxide coated glass with a sheet resistance of 11 Ω/ purchased from a Libby-Owen-Ford (LOF) were used as substrates. The samples were thoroughly cleaned with methanol prior to substrate mounting. During deposition the gas flow rates were set and then forward rf power turned on to initiate the plasma. The reverse rf power was then minimized using the matching network. Deposition time ranged between one to ten minutes. Since depositions were carried out at room temperatures no time was needed to allow the chamber to cool, and samples were often prepared in a consecutive manner.

Deposition took place on both the grounded or powered electrode. Deposition on the powered electrode was carried out by setting the glass or silicon samples on the 5" x 5" stainless steel bottom plate. This plate was electronically isolated from the rest of the chamber by a 0.125" thick Teflon spacer. A grounded steel plate was placed behind the Teflon to prevent a plasma from forming outside the chamber. The grounded electrode consists of the top plate and the four sides of the chamber. For deposition on the

grounded electrode samples were fastened to the cylinder face with small pieces of Kapton tape.

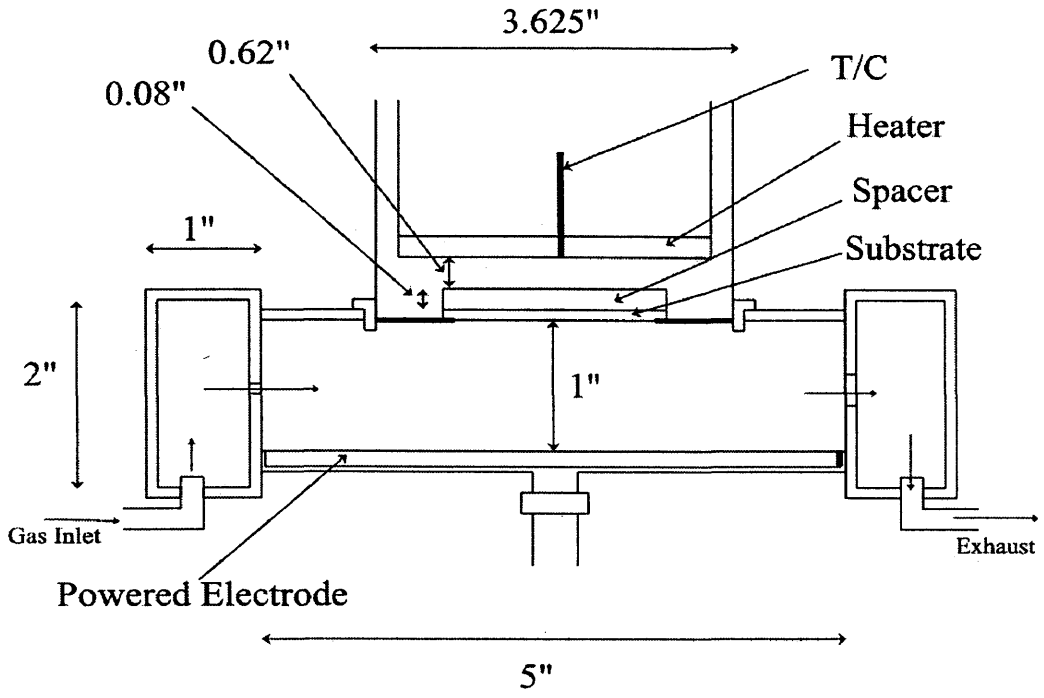

Figure 2.2: Detailed schematic of deposition chamber

The operating parameters and range of setpoints are given in Tables 2.1 and 2.2. Table 2.1 summarizes a range of operating conditions studied for plasma composition in Chapter 3. Table 2.2 was a narrower set of parameters that was examined for optimizing electrochromic performance as discussed in Chapter 4. The base case conditions for WF_6, O_2, and H_2 were 4, 32, and 12 sccm, respectively. One percent Ar was added as an actinometer.

Variable		Base Case	Range
H_2:WF_6 Ratio		3	1-5
O_2:WF_6 Ratio		8	2-26
Total flow rate	[sccm]	48	12-60
Power	[Watts]	200	50-300
Pressure	[mTorr]	200	200-400

Table 2.1: Range of parameters for initial OES and growth rate study

Variables		Setpoints
H_2:WF_6 Ratio		4
O_2:WF_6 Ratio		17
Total flow rate	[sccm]	76
Pressure	[mTorr]	200
Power	[Watts]	50-250

Table 2.2: Parameters used in optimization of electrochromic performance

2.2 Optical Emission Spectroscopy

An Ocean Optics SD2000 spectrometer was used in collection of optical emission. The spectrometer contains two gratings for separation of the wavelengths. One detects a wavelength range from 200-850 nm; the other from 530-1100 nm. A 200 μm bifurcated cable with a 25 μm slit was used. The optical resolution is approximately 1.5 nm. The collection end of the fiber was mounted on the outer window of the larger outside chamber and aligned with the small inner opening to the center of the deposition chamber. The inside window is 0.75", with a 0.5" hole available for the viewing of the plasma. Because the fiber is mounted on the outside of the window, all wavelengths <~300 nm were lost due to absorption in the window.

The main benefit to using OES in studying plasma dynamics is its ability to track relative amounts of atomic species. Inelastic collisions between atoms and electrons in the plasma cause the excitation of ground state species to higher energy levels, which is followed by relaxation and photoemission. The OES spectrum obtained is a complicated function of electron density and the electron energy distribution. To eliminate the dependence on electron density and energy a small amount of an inert gas such as argon is introduced, called an actinometer, which has similar energy dependent cross sections to the species of interest[21]. The relative density may then be evaluated by measurement of the emission intensities of the species of interest and the actinometer as described below

$$[X] \propto [Ar] \frac{I_X}{I_{Ar}} \tag{2.1}$$

Where $[X]$, $[Ar]$, and I_X/I_{Ar} are the species densities and the emission intensities, respectively. Widely used for process control in plasma etching, actinometry has recently been applied to study PECVD systems as well.[22,23] OES was used to track the plasma density of O, H, and F as a function of process conditions. Table 2.3 summarizes the lines used in OES studies. The argon emission at λ=750 nm is a well-established actinometer for both atomic fluorine and atomic oxygen[21,24].

Species	Excitation	Transistion
H	656 nm	$^2P^0$ - ^2D
O	844 nm	^3P - ^3S
F	704 nm	$3p^2P^0$-$3s^2P$
Ar	750 nm	$2p^1$-$2s_2$

Table 2.3: Summary of transitions and excitations used in OES to track H, O, F, and Ar.

2.3 Electrochemical cell configuration

There are several key metrics that are used to quantify the quality of electrochromic tungsten oxide. Optical performance is typically judged using terms such as change in optical density (Δ O.D.) and coloration efficiency. These are extrinsic film parameters that are based on the initial and final state of a film. Dynamics such as response time are also critical, and depend on ion diffusivity and the electromotive force (emf). In this section these terms are defined and related to intrinsic properties. The techniques that have been used to measure them are reviewed, as well as the specific approaches employed in this thesis.

Typically research of electrochromic materials focuses on the deposition, characterization, and optimization of the individual components of an electrochromic device. Characterization of key properties are measured in an electrochemical cell in conjunction with optical transmission. Figure 2.3 shows a schematic of the apparatus used in this work, which is common to this field[25,26]. Samples of tungsten oxide deposited

onto a TCO substrate are suspended in a liquid electrolyte. A Gamry model PC4 Potentiostat modulates the voltage in this conventional three electrode configuration and the current is recorded. The tungsten oxide film serves as the working electrode, a graphite rod was used as the counter electrode, and all measurements were referenced to a saturated calomel electrode. The current was recorded in direct registry with changes in laser intensity to provide a direct of correlations between ion intercalation and optical properties.

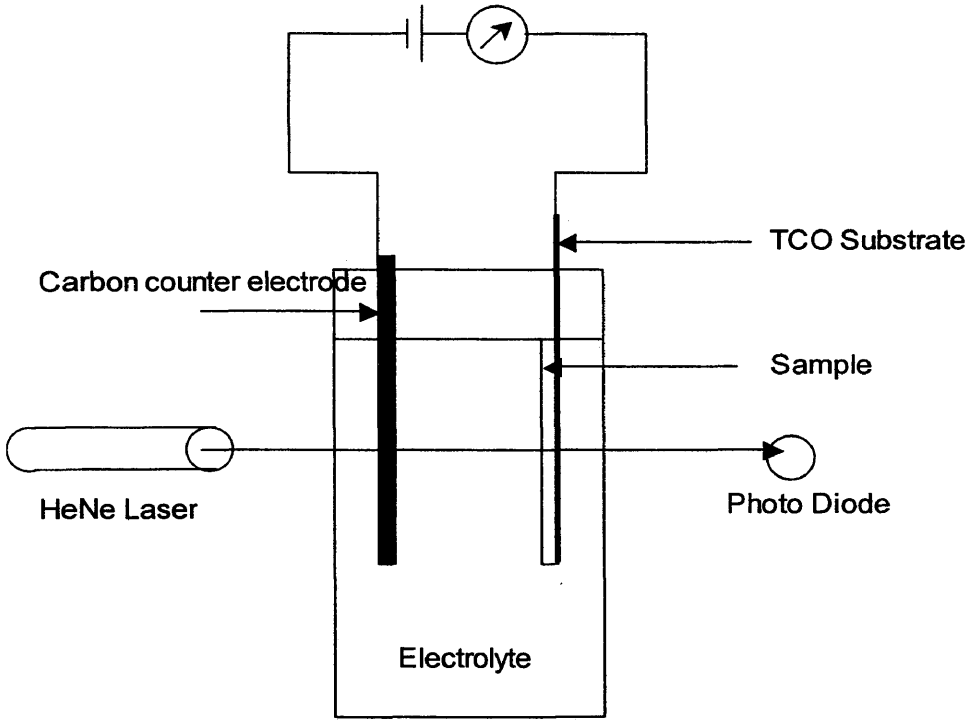

Figure 2.3: Diagram of the three-electrode electrochemical cell configuration used in evaluation of electrochromic performance.

2.4 Electrochemical evaluation

In an electrochemical cell, the transmission of tungsten oxides switches from transparent to opaque in response to a small applied voltage. This process is based on the double injection of light ions and electrons to form the tungsten bronze M_xWO_3. Several mechanisms have been suggested as the limiting step in the formation of the tungsten bronze [27]

1. the series resistance in the cell that limits ion transfer to the surface [26,28]
2. a barrier to the charge transfer at the WO_3/electrolyte interface[29-31]
3. diffusion of ions within the electrochromic film [31-33]

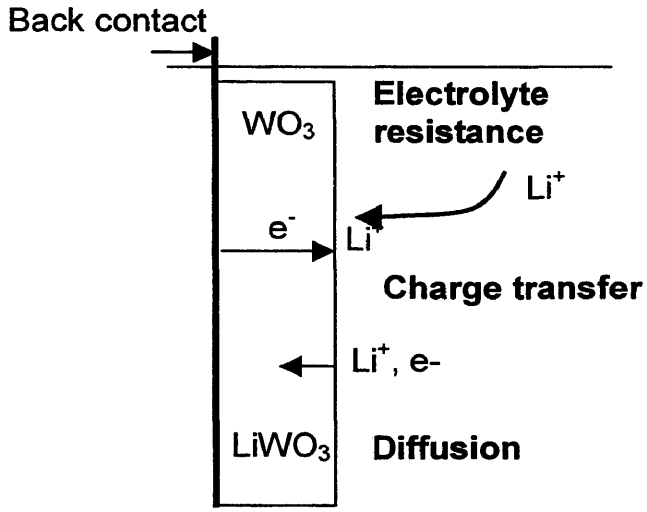

$$WO_3 + xLi^+ + xe^- \leftrightarrow Li_xWO_3$$

Figure 2.4: Summary of suggested limiting mechanisms to the formation of the tungsten bronze

This section reviews the three electrochemical techniques of AC impedance spectroscopy, cyclic voltammetry (CV), and the potentiostatic intermittent titration technique (PITT) commonly employed in the literature for evaluation of the process depicted in Figure 2.4. In all three methods, either current or voltage may be the dependent variable, but this thesis will only address the case of controlled voltage. Accordingly, all three characterization approaches rely on analysis of the current response to obtain information on electrolyte resistance, charge transfer kinetics, or diffusion. Differences arise between the techniques as to the form of the applied voltage and the resulting data that each produces. Figure 2.5 summarizes the different applied waveforms and responses of these techniques.

In AC techniques, a constant voltage is applied to the working electrode and a small alternating voltage signal is superimposed on top of the static signal. In the case of WO_3, the constant applied voltage fixes the intercalation state of the film. The phase and magnitude of the induced current as a result of the alternating signal is measured. The measured impedance is typically presented in a Nyquist plot such as that shown in Figure 2.5. By recording the current over a wide range of frequencies, the different processes limiting the formation of the tungsten bronze may be separated out through their different time constants.

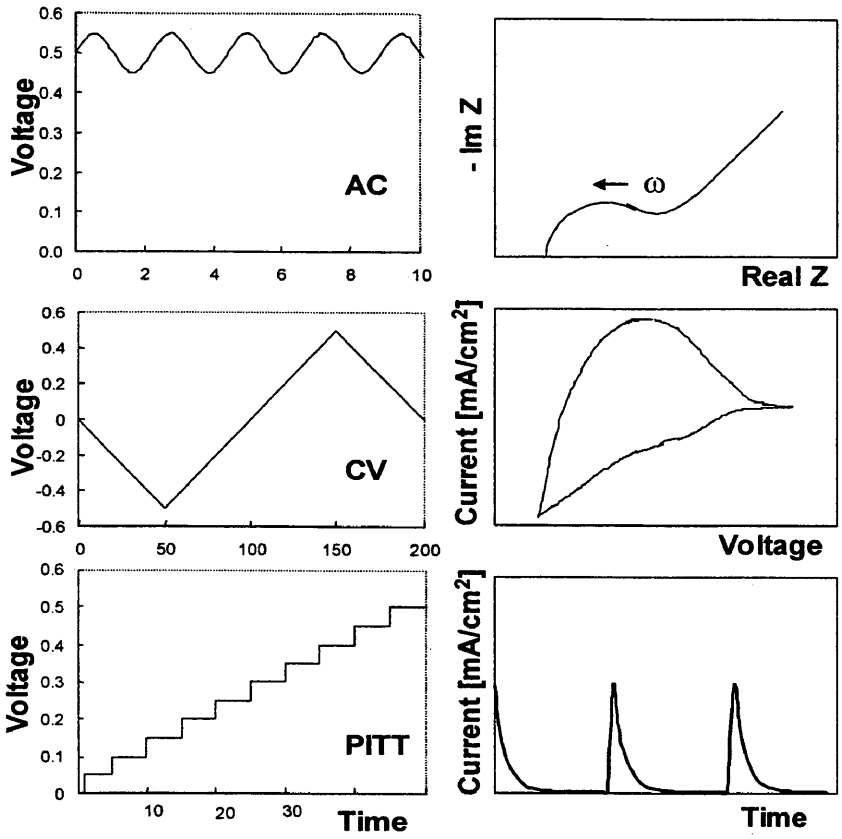

Figure 2.5: Summary of applied waveforms in AC, CV, and PITT characterization techniques and typical responses used in analysis.

Cyclic voltammetry is similar to AC techniques; however the applied waveform is a saw-tooth shape as opposed to a sinusoid. The voltage is modulated between initial and final states at a given sweep rate. The resulting plot of current vs. voltage, known as a cyclic voltagramm can also be analyzed to obtain information on reaction kinetics and diffusion. However, most often in the evaluation of electrochromic films, CV analysis

serves most usefully as a fingerprint technique for comparison between samples and evaluating the cycle stability.

In PITT, a small potential step is applied to the film and the induced current decay in time is recorded. This technique relies on small step changes in voltage, thus small changes in composition and intrinsic film properties. By applying sufficiently small steps, one may safely assume that the diffusion coefficient and emf are constant within each step. The diffusion coefficient remains the only variable to be determined and can be fit to an analytical solution for the current response. These three techniques are discussed in more detail below.

2.4.1 AC impedance spectroscopy

The advantage to AC impedance analysis is that if measurements are made over a wide enough frequency range, then different physical processes may be separated out by their different time constants. The alternating current response is analyzed to determine the impedance over a wide range of frequencies. Impedance is the complete complex representation of resistance to an AC signal. In an ideal resistor, the current behaves according to Ohm's law and resistance is defined as:

$$R = \frac{E}{I} \tag{2.2}$$

where R is the resistance, E the applied potential, and I the current. In AC techniques the applied potential is expressed as a function of time, $E(t)$.

$$E(t) = E_o \cos(\omega t) \tag{2.3}$$

where E_o is the amplitude of the signal, and ω is the radial frequency expressed in radians per second. The response signal, *I(t)* is defined by an amplitude, I_o and a phase shift, ϕ.

$$I(t) = I_o \cos(\omega t - \phi) \tag{2.4}$$

An expression analogous to Ohms law for impedance of the system is expressed as:

$$Z = \frac{E_o \cos(\omega t)}{I_o \cos(\omega t - \phi)} \tag{2.5}$$

In analysis of electrical circuits subjected to an AC signal, it is convenient to represent impedance as a complex function through use of Euler's relationship. The applied potential can be described as the following complex function,

$$E(t) = E_o \exp(i\omega t) \tag{2.6}$$

and the current response as,

$$I(t) = Io \exp(i\omega t - i\phi)\,. \tag{2.7}$$

The impedance represented as a complex number using Euler's relationship is then

$$Z = \frac{E}{I} = Z_o \exp(i\phi) = Z_o(\cos\phi + i\sin\phi)\,. \tag{2.8}$$

The preceding equation for the impedance as a function of frequency consists of a real and imaginary component. AC impedance spectroscopy measures the impedance as a function of frequency and the resulting impedance data is displayed on a complex plot, referred to as a Nyquist plot. The x-axis depicts the real component and the y-axis the

imaginary component, each point represents a constant frequency. Figure 2.6 is an example of such a plot.

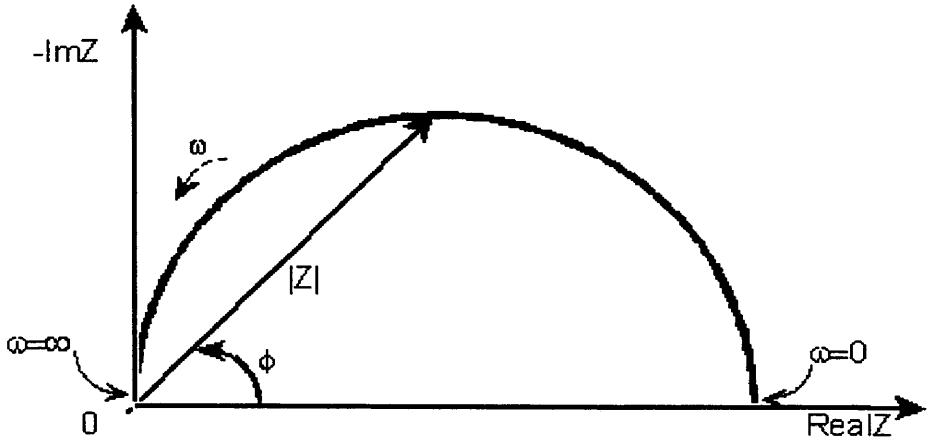

Figure 2.6: Example of a Nyquist plot obtained from AC impedance spectroscopy.

AC impedance analysis relies on fitting the experimental impedance data to an equivalent circuit that represents the electrochromic cell. This equivalent circuit consists of resistors, capacitors, and inductors that have a physical basis in the process dynamics of the electrochemical cell. For example, electrolyte resistance in the cell is commonly modeled as an ideal resistor. The equivalent circuit for diffusion of a metal into an oxide electrode, assuming the diffusion is controlled by a concentration gradient as opposed to an electric field, is the traditional Randles circuit[34]. The Randles circuit simulates the AC response of a system subjected to both charge transfer and diffusion limited considerations. Figure 2.7 is a schematic of the elements that make up a Randles circuit; R_{cell} represents the cell resistance that is characteristic of the experimental apparatus, C_{DL},

the capacitive effect of double layer electrode-electrolyte interface, R_{CT}, the kinetic charge transfer resistance, and Z_D, a complex frequency dependence arising from diffusion of the ion into the film.

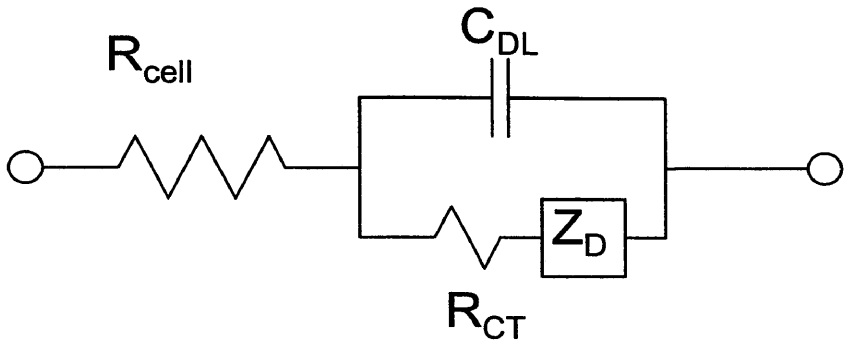

Figure 2.7: Randles equivalent circuit for the AC response of a system subject to both kinetic and diffusion limiting regimes.

The frequency response of this circuit will be governed by the relative importance of charge transfer and diffusion in determining the current. An electrode reaction rate may be controlled by diffusion at long times (low frequencies) and cell resistance at high frequencies (short times). By determining the best fit values for the different circuit elements, the AC impedance technique is very useful in determining the magnitude of the different processes limiting the formation of the tungsten bronze. Figure 2.8 contrasts Nyquist plots for an electrochemical cell under either strict diffusion control or mixed charge transfer and diffusion control. Figure 2.8(a) depicts the complex plane representation for an EC cell that is almost entirely subject to diffusion control. The high

frequency real axis intercept gives the value of the electrolyte resistance, and the diffusion coefficient may be determined from the slope of the straight line portion of the plot. In Figure 2.8(b) a transition is obtained when the kinetics pass from charge transfer limited control at high frequencies to diffusion control at low frequencies. The semi-circle is a consequence of the parallel combination of C_{DL} and R_{CT}. The extrapolated second real axis intercept represents the cumulative effect of both the electrolyte and charge transfer resistance.

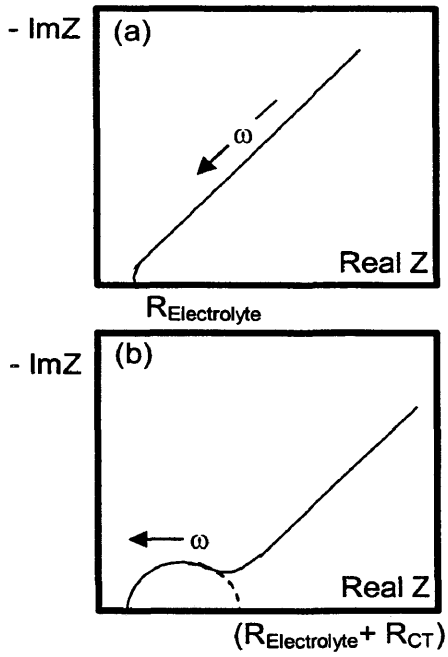

Figure 2.8: Nyquist plot depicting diffusion control (a) and mixed charge transfer and diffusion control (b).

The Randles equivalent circuit has established itself as an effective model for electrochromic film evaluation[32,33,35]. However, one a critical drawback to this technique is the length of time required to measure impedance over a frequency range that typically spans several orders of magnitude. In addition, this experiment would need to be repeated at many baseline voltages to understand the significance of ion intercalation. Due to these limitations CV and PITT techniques were employed. As shown in Chapter 3, cyclic voltammetry provides a convenient qualitative evaluation of film performance. In Chapter 4, PITT is used to quantify diffusion coefficients. These techniques are described in more detail below.

2.4.2 Cyclic voltammetry

In cyclic voltammetry, a voltage between the tungsten oxide contact and the counter electrode ramps linearly between two extreme values at a fixed sweep rate. The electrical currents associated with intercalation/deintercalation of the charged species are recorded. Example cyclic voltagramms, are shown in Figure 2.9(a) for sweep rates of 50, 125, and 250 mVolts/second between a voltage range of 0.5 Volts and -0.5 Volts in a 1M H_2SO_4 electrolyte. The corresponding in-situ change in laser intensity is also shown in Figure 2.9(b). Increasing the sweep rate generates an increasing current density and a decreased change in transmission. Faster sweep rates do not allow time for ions to fully diffuse into the film. However, quantitative estimates of diffusion coefficients from cyclic voltagramms are not typically obtained. Instead, the technique is used as a

qualitative fingerprint for the electrochemical process. The current vs. voltage response provides a means to evaluate what potentials yield stable operation and trace reversible and irreversible effects.

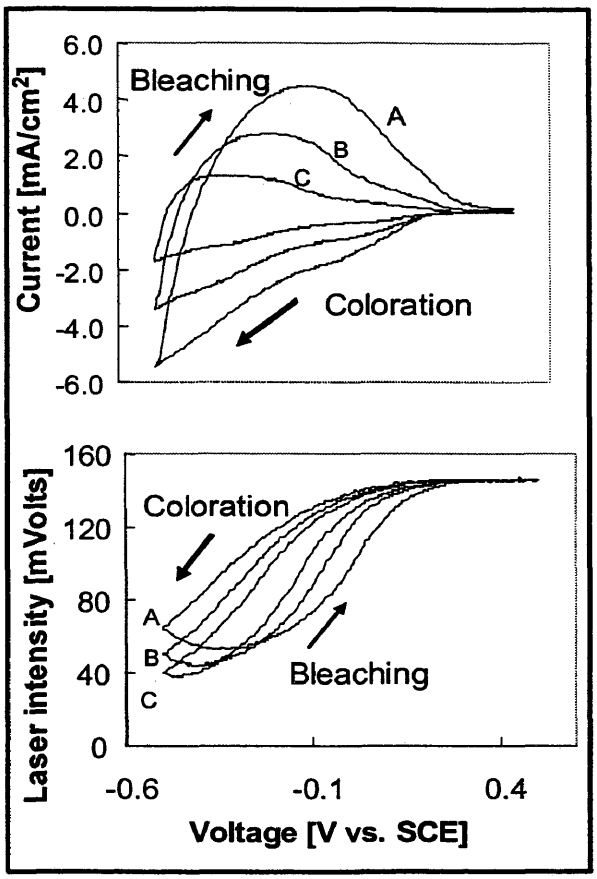

Figure 2.9: Examples of cyclic voltagrams of tungsten oxide at three sweep rates, (A) 250 mVolts/second, (B) 125 mVolts/second, and (C) 50 mVolts/second. The corresponding optical response is shown in the bottom figure.

In particular, the technique of cyclic voltammetry provides a convenient approach to evaluate three key performance metrics critical to smart window performance. First, the contrast ratio can be determined from the ratio of the transmission in the clear state to that of the darkened state. Second, the switching time may be qualitatively estimated by altering the sweep rate. Furthermore, the contrast ratio as a function of switching time is easily obtained from the cyclic voltagramm. Finally, issues related to long term stability from continuous cycling can be observed as the CVs evolve from the original and n^{th} cycled trace. For these reasons, cyclic voltammetry is a useful tool for evaluation of electrochromic performance.

2.4.3 Potentiostatic Intermittent Titration Technique

During electrochromic coloration, intercalation of ions causes a change in the film's chemical potential that is typically described by the electromotive force (*emf*). *emf* is defined by the following fundamental equation

$$emf = \frac{-\Delta G}{F} \tag{2.9}$$

where ΔG is the change in free energy associated with the transfer of a charged species from the electrolyte into the WO_3 film, and F is Faraday's constant. Faraday's constant simply converts the change in free energy to a voltage. The Nernst equation can be used to describe the changes in *emf* as a result of the transition of Li^+ from the electrolyte to neutral Li in intercalated Li_xWO_3.

$$emf = E_o + \frac{RT}{F}\ln\left(\frac{Li^+}{Li}\right) \tag{2.10}$$

where E_o is the standard electrode potential, T is temperature, and R is the universal gas constant.

The current response as a result of ion intercalation and *emf* can be described as

$$i = \frac{V_a - emf(x)}{R} \tag{2.11}$$

where V_a is the applied potential and R is a series resistance. An applied step potential causes ions to move into the film until a resulting *emf* is established that negates the applied potential. In this regard, a change in potential sets a new equilibrium intercalation level, and the current response describes the transient flux of ions required to reach the new condition. The extent of intercalation, x is experimentally determined by integrating the current vs. time response to determine the amount of ions that moved into the film. The current behavior is a direct measure of the flux of ions entering the film as described by

$$FD\frac{\partial C}{\partial z}\bigg|_{z=l} = i = \frac{V_a - emf(x)}{R} \tag{2.12}$$

where the derivative is evaluated at the electrode/electrolyte interface.

To estimate the diffusion coefficient one seeks a solution to Fick's second law subject to appropriate boundary and initial conditions that will best fit the observed current response to a step change in potential. Equation 2.12 serves as a boundary

condition at the electrode/electrolyte interface. A no-flux boundary condition is met at the back contact/WO_3 interface and initially no intercalation has taken place.

$$\frac{\partial C}{\partial t} = \frac{\partial}{\partial z}\left(D\frac{\partial C}{\partial z}\right) \tag{2.13}$$

$$C = 0 \qquad 0 < z < L \qquad t=0 \tag{2.14}$$

$$\left.\frac{\partial C}{\partial z}\right|_{z=L} = 0 \qquad z=L \qquad t>0 \tag{2.15}$$

$$FD\left.\frac{\partial C}{\partial z}\right|_{z=0} = \frac{V_a - emf(x)}{R} \qquad z=0 \qquad t>0 \tag{2.16}$$

Solution to the above equation requires a numerical approach as well as knowledge of *emf(x)* and the series resistance. Potentiostatic intermittent titration technique (PITT) is an approach that provides an analytical solution to Fick's second law and does not require the *emf* or series resistance to be determined. By applying sufficiently small steps, one may safely assume that the diffusion coefficient and *emf* are constant within a step. Under these conditions, Fick's law and boundary conditions are simplified to the following

$$\frac{\partial C}{\partial t} = D\left(\frac{\partial^2 C}{\partial z^2}\right) \tag{2.17}$$

$$C = C_o \qquad 0 < z < L \qquad t=0 \tag{2.18}$$

$$\left.\frac{\partial C}{\partial z}\right|_{z=L} = 0 \qquad z=L \qquad t>0 \tag{2.19}$$

$$C=C_s \qquad z=0 \qquad t>0 \tag{2.20}$$

These conditions give rise to the following analytical solution to Fick's second law, [36,37] and associated current response:

$$C(z,t) = C_s - (C_s - C_o)\frac{4}{\pi}\sum_0^\infty\left[\frac{1}{2n+1}\sin\left(\frac{(2n+1)\pi z}{2L}\right)\exp\left(-\frac{(2n+1)^2\pi^2 Dt}{4L^2}\right)\right] \quad (2.21)$$

$$I(t) = \frac{2nF(C_s - C_o)D}{L}\sum_0^\infty\exp\left(-\frac{(2n+1)^2\pi^2 Dt}{4L^2}\right) \quad (2.22)$$

Given the known values of C_s and C_o, the diffusion coefficient was varied to best match the current response of each step. PITT is an approach that greatly simplifies the effects of *emf* and provides a simple experimental means to estimate the diffusion coefficient.

2.5 Optical properties

2.5.1 Measurement of the absorption coefficient and calibration of laser intensity

Optical performance was assessed using a He-Ne laser operating at a wavelength of 633 nm. The laser was directed through the suspended sample at normal incidence for *in-situ* measurement of transmission changes. Comparison of absolute measures from sample to sample was problematic due to variations in initial laser intensity resulting from sample placement. However, Beer's law, which uses relative measurements, proved

to be an effective means to analyze the laser intensity data. The laser intensity measured in mV from the photodiode was fit to Beer's law.

$$I = I_o \exp(-\alpha L) \qquad (2.23)$$

where I_o is the initial intensity of the He-Ne laser, I the final intensity, L the thickness of the film in cm, and α the intercalation degree dependent absorption coefficient in cm^{-1}. The absorption coefficient as a function of intercalation was measured in a series of experiments similar to PITT. To vary extent intercalation, the voltage applied to the working tungsten oxide electrode was modulated in a series of steps and allowed to reach equilibrium. Measurements of the initial and end point laser intensity from each step were used to determine the absorption coefficient as a function of intercalation.

Absolute changes in transmission as a function of intercalation were carried out using a Cary 5G UV-Vis-NIR spectrophotometer. In the spectrophotometer the contribution of the LOF substrates was subtracted out, providing measurements indicative of the WO_3 film alone. Figure 2.10 shows the absolute transmission of a representative sample as a function of wavelength from 300 nm to 1000 nm at varying degrees of intercalation of x=0.00 to x = 0.16.

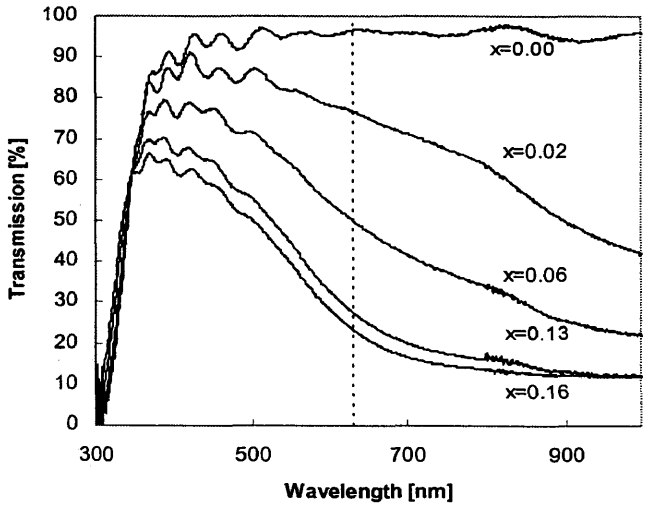

Figure 2.10: Absolute transmission values for a representative sample under varying degrees of intercalation. The dashed line represents the wavelength of the He-Ne laser operating at 633 nm.

From these measurements, a linear relationship was observed between absolute transmission at 633 and the photodiode signal. A calibration curve relating changes in laser intensity to absolute transmission values is depicted in Figure 2.11.

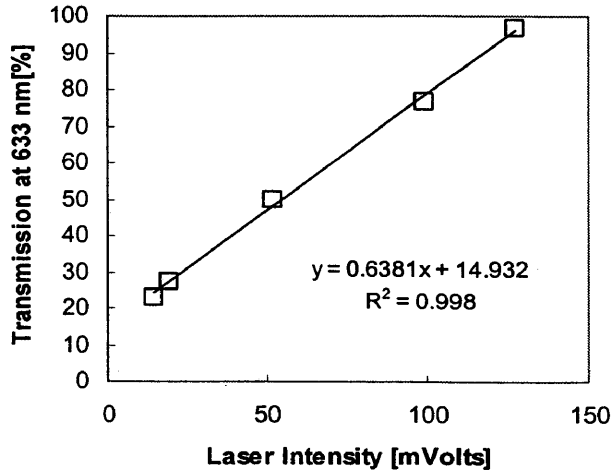

Figure 2.11: Calibration of laser intensity to absolute transmission.

2.5.2 Change in optical density and coloration efficiency

The absorption coefficient is an intrinsic property of the PECVD grown films of tungsten oxide. However, changes in transmission in the literature in are usually reported in terms of a change in optical density (ΔOD). The change in optical density is defined as:

$$\Delta OD = \log\left(\frac{T_b}{T_c}\right) \tag{2.24}$$

where T_b and T_c are wavelength dependent transmission values of the bleached and colored states, respectively. Coloration efficiency is also often reported as simply the change in optical density divided by the total intercalated charge required to reach T_c. Coloration efficiency is expressed as follows:

$$CE = \frac{\Delta OD}{Q} \tag{2.25}$$

where Q is in Coulombs/cm^2 and CE is typically expressed in cm^2/C. Literature ranges of these parameters for WO_3 typically lie between 1 - 4 for ΔOD[25] and 37 - 260 cm^2/Q for CE[9]. Both ΔOD and CE are employed for electrochromic evaluation, but are not intrinsic film properties and depended on numerous parameters including extent of intercalation and film thickness.

2.5.3 Variable Angle Spectroscopic Ellipsometry

Variable angle spectroscopic ellipsometry (VASE) was used to accurately measure film thickness and determine the index of refraction of PECVD WO_3. The J.A. Woollam Co. Inc. WVASE32 system was used for all thickness and index of refraction measurements. The system has a spectral range from 190 nm to 1700 nm and the angle of incidence may be varied from 5° to 85°. For characterization of tungsten oxide films in this thesis the angle of incidence was set to 70° and measurements were taken over the range of 400 nm to 1200 nm.

Ellipsometry measures the change in the polarization state of light reflected from the surface of the sample. The measured values are expressed as psi(Ψ) and delta(Δ). These values are related to the ratio of Fresnel reflection coefficients R_p and R_s for p and s polarized light. R_p is the ratio of reflected parallel component of the electric field to the

incident parallel component of the electric field. R_s is the same ratio of the perpendicular components. Δ and Ψ are related to R_s and R_p by

$$\rho = \frac{R_p}{R_s} = \tan(\Psi)\exp(i\Delta) \tag{2.26}$$

After obtaining the experimentally measured values of Δ and Ψ versus wavelength, the data is fit using a Cauchy model to describe the refractive index variation with wavelength. Unknown parameters of thickness and refractive index are varied until the root mean square error is minimized. The Cauchy model simply represents the wavelength dependent real component of the index of refraction by the following equation:

$$n(\lambda) = A + \frac{B}{\lambda^2} + \frac{C}{\lambda^4} \tag{2.27}$$

In this model, the film is assumed to be non-absorbing and the index of refraction consists of only a real component. For pure films of tungsten oxide the Cauchy model has been shown to be an appropriate choice for representing the wavelength dependent refractive index[38].

2.5.4 Estimation of porosity

The index of can be a used as an estimation of film porosity. The porosity may be estimated from the following relationship:

$$Porosity(\%) = 100 \times \frac{(n_m - n_o)}{(1 - n_o)} \tag{2.28}$$

where n_m and n_o are the measured and intrinsic refractive indices, respectively. In order to accurately predicted porosity values, a value for the intrinsic refractive index must be known. In this work, an intrinsic index value of $n_o = 2.4$ at a wavelength of 400nm was taken from the literature[39].

2.6 AFM imaging

The difference in ion bombardment between films deposited on the grounded versus powered electrode for both TCO coated glass and silicon substrates was characterized using AFM imaging. Figure 2.12 compares AFM images of films deposited simultaneously on the grounded and powered electrode for silicon substrates under the base case conditions given in Table 2.1. The powered electrode sample is dense and smooth, characterized by an index of refraction of 2.20 and a roughness of 1 nm, while the grounded electrode film is more porous and has a very different structure, and characterized by an index of refraction of 2.05 and a roughness of 3 nm. The influence of ion bombardment on electrochromic performance is discussed in detail in Chapters 3 and 4.

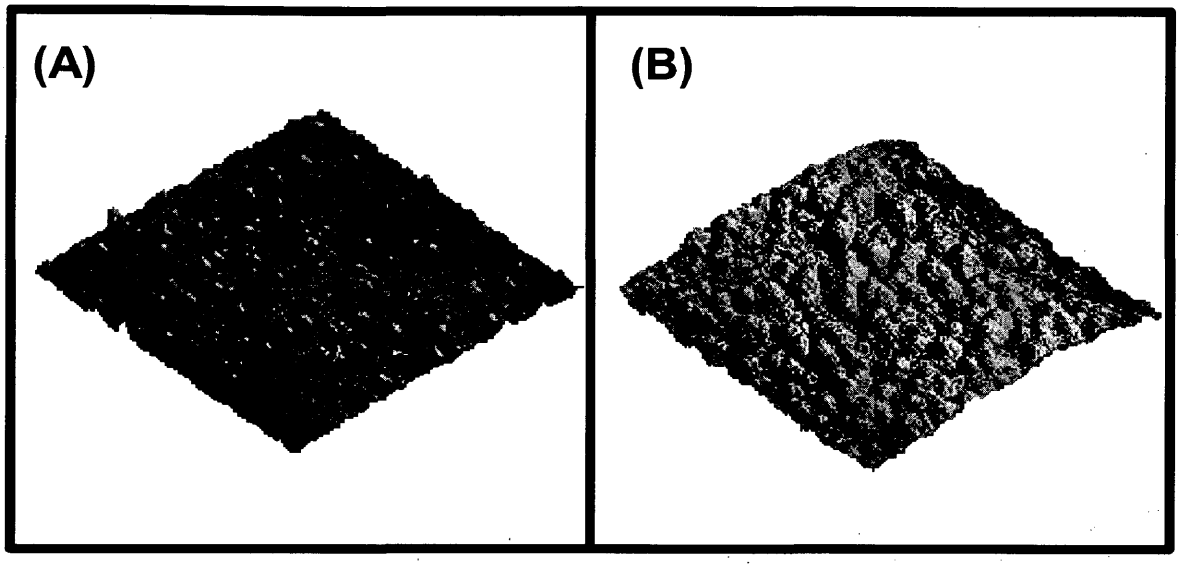

Figure 2.12: AFM comparison between samples grown on powered vs. grounded electrode. Sample A: Roughness 1 nm, Index of refraction at 400 nm 2.20

Sample B: Roughness 3 nm, Index of refraction at 400 nm 2.05

The initial roughness of the TCO coated substrate was characterized using AFM imaging and found to be 40 nm. Two films were deposited on TCO substrates under base case conditions on both the powered and grounded electrode. The sample grown on the powered electrode was deposited at 250 watts, while the sample prepared on the grounded electrode was deposited at 150 watts. Figure 2.13 summarizes the AFM images and roughness values for the TCO substrate and deposited WO_3 films. The roughness values for samples grown on the powered and grounded electrode were found to be 24 nm and 7.4 nm, respectively. In both cases, the resulting surfaces show a substantial decrease in surface roughness compared to the original TCO substrate. The films grown

on the grounded electrode were 3X smoother then the powered. It is interpreted that the increased ion bombardment on the powered electrode causes the WO_3 to more closely mirror the underlying substrate.

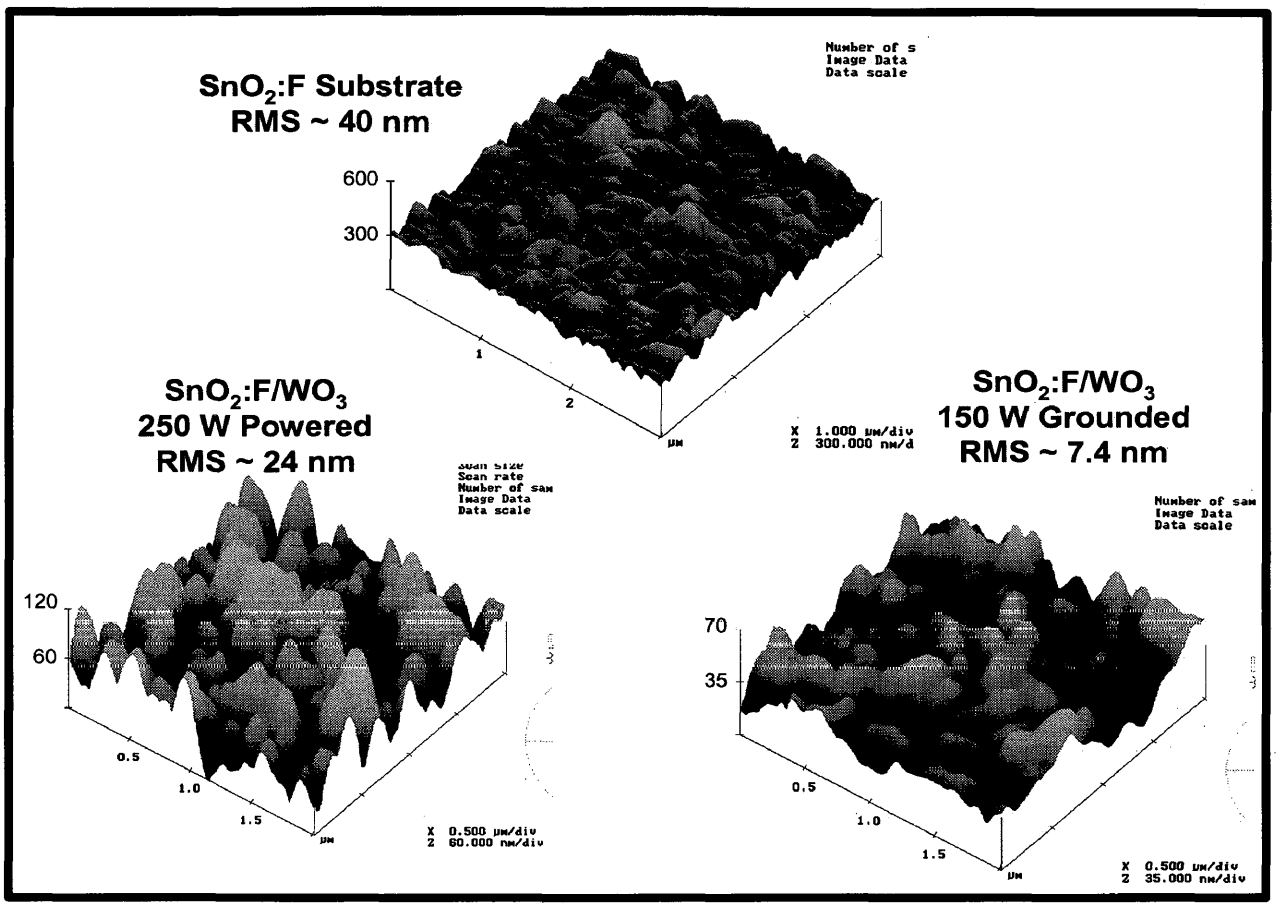

Figure 2.13: AFM images and roughness values of the TCO coated substrate and deposited films.

CHAPTER 3

AN INVESTIGATION OF THE ROLE OF PLASMA CONDITIONS ON DEPOSITION RATE AND ELECTROCHROMIC PERFORMANCE OF TUNGSTEN OXIDE THIN FILMS

The following is a reproduction of a paper published in The Journal of Vacuum Science and Technology A, Volume 21, Issue 6, pp. 1927-1933, 2003. This chapter is reproduced as is except that section numbers, references, and figures were changed to conform to the thesis format.

Michael Seman and Colin A. Wolden*
Department of Chemical Engineering, Colorado School of Mines, Golden, CO 80401

Abstract

Plasma-enhanced chemical vapor deposition (PECVD) has been used to form electrochromic tungsten oxide thin films from gas mixtures of WF_6, O_2, and H_2. The chemistry of this system was investigated using optical emission spectroscopy (OES). The plasma composition and deposition rate were examined as a function of operating conditions. Growth rates were maximized when the atomic fluorine density was attenuated and the atomic oxygen density was saturated. With the exception of hydrogen scavenging of fluorine radicals, the major reaction pathway was simply dissociation, as the densities of the atomic species were proportional to the initial reagent composition. An apparatus was built to evaluate electrochemical performance in direct registry with

* Corresponding Author: cwolden@mines.edu

optical transmission. This characterization technique was used to demonstrate that ion bombardment has a dramatic impact on electrochromic performance. Ion bombardment was found to increase film density, as inferred from measurements of the refractive index. Efficient hydrogen intercalation was observed only in those films whose refractive index at 400 nm were less than 2.1. Finally, it was shown that a tungsten oxide thickness of ~600 nm was optimal with respect to contrast ratio.

3.1 Introduction

Tungsten oxide is a leading electrochromic material that is being pursued for numerous applications including sensors,[40,41] "smart" windows,[42] and display technology.[4] Solid-state electrochromic devices are composed of a stack of thin metal oxides whose optical transmission may be reversibly altered between clear and opaque in response to an applied voltage. The stack consists of an ion storage layer, an electrolyte, and an electrochromic layer sandwiched between two transparent conducting oxide (TCO) electrodes.[4] Electrochromic materials demonstrating cathodic coloration are darkened upon intercalation of the light ion, H^+ or Li^+. When a small voltage is applied across the electrodes, an ion is pulled from the storage layer across the electrolyte and inserted into the electrochromic. In the case of tungsten oxide the electrochemical insertion/extraction of ion A^+ can be written as

$$WO_3 + x\,(A^+ + e^-) \leftarrow \rightarrow A_xWO_3 \qquad (3.1)$$

Numerous materials exhibit electrochromic behavior[43], but tungsten oxide has been the most successful and widely studied over the last three decades[1].

Physical vapor deposition (PVD) techniques such as evaporation[44] and sputtering[38,40,41] have been most commonly used for thin film synthesis to date. In addition, reactive approaches such as chemical vapor deposition (CVD)[10,11] and sol-gel methods have also been explored.[12] Plasma-enhanced chemical vapor deposition (PECVD) offers an attractive alternative due to its high deposition rates and low temperature capability. Thermal CVD deposition is activated by a heated substrate, which in the case of WO_3 requires substrate temperatures in excess of 200 °C.[10,11] In a plasma high-energy electrons dissociate, excite, and ionize the gaseous precursors, allowing room temperature deposition[15,16]. Established as the primary synthesis technique for silicon oxide in integrated circuit manufacturing, PECVD has been extended to deposit numerous metal oxide thin films. [45-47] PECVD was first demonstrated for WO_3 synthesis by Tracy and Benson[15] in 1986, but has subsequently received relatively limited attention[16]. PECVD offers advantages for large area uniformity, and it is not susceptible to issues associated with target aging that can limit PVD techniques [41]. Our group has developed PECVD processes for the synthesis of TCO electrodes[17-19]. In concept, PECVD could be used for synthesis of a complete electrochromic device by simply alternating process chemistries. Simplified processing would enhance the cost-effectiveness of this technology.

PECVD typically employ mixtures of the three reactants WF_6, O_2, and H_2. Tungsten hexafluoride decomposes readily, however the reaction is reversible as the released fluorine radicals etch the film. To mitigate this issue hydrogen is added to scavenge atomic fluorine, forming HF. The global reaction may be expressed simply as

$$WF_6 + \text{Excess } O_2 + \text{Excess } H_2 \rightarrow WO_3 + HF + (H_2, O_2, H_2O) \qquad (3.2)$$

However, the details of the plasma chemistry can be highly complex, and the kinetics largely unknown. Henley and Sacks[16] focused on the role of reactant composition, showing that both the H_2:WF_6 and the O_2:WF_6 ratios must be greater than unity in order to achieve high rates and quality films. In this work, optical emission spectroscopy (OES) and electrochromic evaluation have been used to quantify the process-property-performance relationships for this system. This paper provides a comprehensive comparison of plasma composition and growth rate. In addition, evaluation of electrochromic properties was conducted through simultaneous measurement of the electrochemical and optical response of the films. This approach was used to quantify intercalation dynamics and to assess the role of the plasma environment on electrochromic performance. In this paper we demonstrate the important role of ion bombardment on film properties, and optimize film thickness was with respect to contrast ratio.

3.2 Experimental

Deposition of tungsten oxide was performed in a parallel plate, capacitively-coupled plasma chamber. Power was supplied by a 300W rf power supply operating at 13.56MHz and coupled using a matching network. Further details of this custom built chamber are provided in the literature[17]. All depositions were done at ambient temperature using mixtures of tungsten hexafluoride, oxygen, and hydrogen. One percent argon was added as an actinometer. The plasma emission was collected using an optical fiber mounted onto a view port aligned with the center of the plasma. The optical signal was directed into an Ocean Optics SD2000 spectrometer that quantified the emission over the range of 570-1120 nm with a resolution of approximately 1 nm.

Inelastic collisions with electrons in the plasma cause the excitation of ground state species to higher energy levels, which is followed by relaxation and photoemission. The OES spectrum obtained is a complicated function of electron density and the electron energy distribution. To eliminate the dependence on electron density and energy a small amount of an inert gas such as argon is introduced, called an actinometer, which has similar energy dependent cross sections[21]. The relative density may then be evaluated by measurement of the emission intensities of the species of interest and the actinometer as described below

$$[X] \propto [Ar] \frac{I_X}{I_{Ar}} \tag{3.3}$$

Where $[X]$, $[Ar]$, and I_X/I_{Ar} are the species densities and the emission intensities, respectively. Widely used for process control in plasma etching, actinometry has recently been applied to study PECVD systems as well.[22,23] OES was used to track the plasma density of O, H, and F as a function of process conditions. The argon emission at λ=750 nm is a well-established actinometer for both atomic fluorine and atomic oxygen[21,24]. The plasma emission spectrum obtained at the base case conditions is shown in Figure 3.1. The atomic fluorine signal was very weak in all cases, and is shown in the inset. The emission lines used for actinometry are highlighted on the graph and summarized in Table 3.1.

Species	Excitation	Transistion
H	656 nm	$^2P^0$ - ^2D
O	844 nm	^3P - ^3S
F	704 nm	$3p^2P^0$-$3s^2P$
Ar	750 nm	$2p^1$-$2s_2$

Table 3.1: Summary of atomic emission lines used in this work and their electronic transitions.

Silicon wafers and transparent conducting tin oxide coated glass with a sheet resistance of 11 Ω/ purchased from a Libby-Owen-Ford (LOF) were used as substrates. Polished silicon served as an ideal substrate for film thickness and refractive index measurements using spectroscopic ellipsometry, while the LOF glass was used to evaluate electrochromic performance. Spectroscopic ellipsometry was used to measure

the thickness of the films using a J.A. Woolam ellipsometer and the WVASE32 software. Scans were taken over the range of 400-1200nm at 70° angle of incidence. The wavelength-dependent optical constants were fitted using a Cauchy model, which has been successfully employed for tungsten oxide films[38].

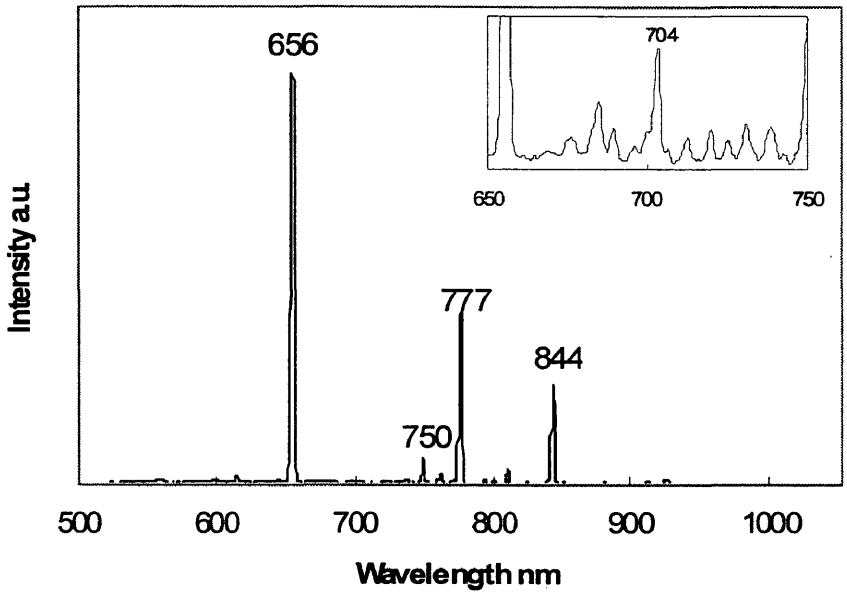

Figure 3.1: An OES spectrum of the base case plasma. The prominent Ar, O, H, and F emission lines used for actinometry are at 750 nm, 844 nm, 656 nm, and 704 nm, respectively.

Film performance was characterized using a custom built apparatus capable of simultaneously analysis of optical and electrochemical performance[44]. A schematic diagram of this setup is shown in Figure 3.2. A deposited film was suspended in an electrolyte solution of either 1M H_2SO_4 or 1M lithium perchlorate in propolyene

carbonate. Cyclic voltammetry (CV) measurements were performed using a Gamry model PC4 Potentiostat. The working electrode was contacted to the TCO, while a graphite rod served as the counter electrode. All measurements were referenced against a saturated calomel electrode. A HeNe laser was directed at normal incidence through the electrochromic film, and the transmitted intensity was evaluated using a Thorlabs DET110 photodiode. Both diagnostics were interfaced through a PC so that optical and electrochemical performance could be monitored in direct registry.

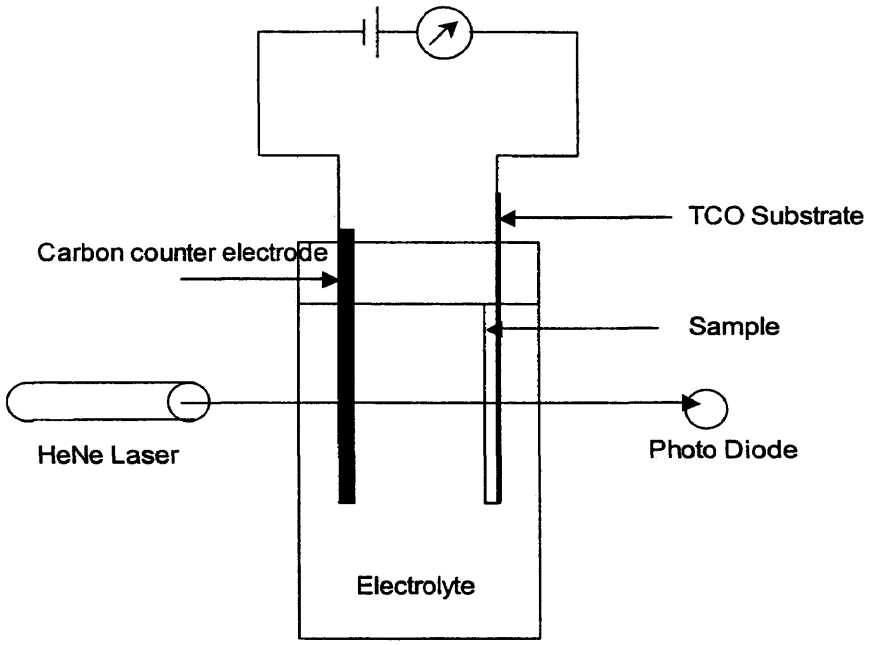

Figure 3.2: Diagram of the apparatus used for taking measurements of optical transmission and electrochemical properties in registry.

3.3 Results and Discussion

3.3.1 Deposition Rate and Plasma Composition

Figures 3.3 through 3.6 compare the deposition rate with the relative densities of the O, H, and F under varying process conditions. The parameters examined include the H_2:WF_6 ratio, the O_2:WF_6 ratio, the total flowrate, rf power, and pressure. The base case parameters and ranges examined are summarized in Table 3.2. Each parameter was varied individually while keeping all of the other values fixed at the base case condition. Similarly, all actinometry values reported here were normalized relative to their values at the base case condition to permit ease of comparison among figures.

Variable		Base Case	Range
H_2:WF_6 Ratio		3	1-5
O_2:WF_6 Ratio		8	2-26
Total flow rate	[sccm]	48	12-60
Power	[Watts]	200	50-300
Pressure	[mTorr]	200	200-400

Table 3.2: Summary of the base case parameters and the ranges examined in this work.

Figure 3.3 compares the plasma composition and growth rates for films grown as a function of H_2:WF_6 ratio. For values of H_2:$WF_6 \leq 1$ no deposition was observed. The atomic fluorine density was ~7X greater than the base case, confirming that these radicals were present in enough abundance to etch the film. The deposition rate increased sharply

as the H_2:WF_6 ratio was increased from 1 to 3. For values H_2:$WF_6 \geq 3$ the fluorine density was attenuated, and the growth rate saturated. With increasing H_2:WF_6, a small increase in H density was observed that also saturated at a H_2:WF_6 ratio ≥3. The atomic O signal decreased slightly over the range examined, which was consistent with the degree of dilution.

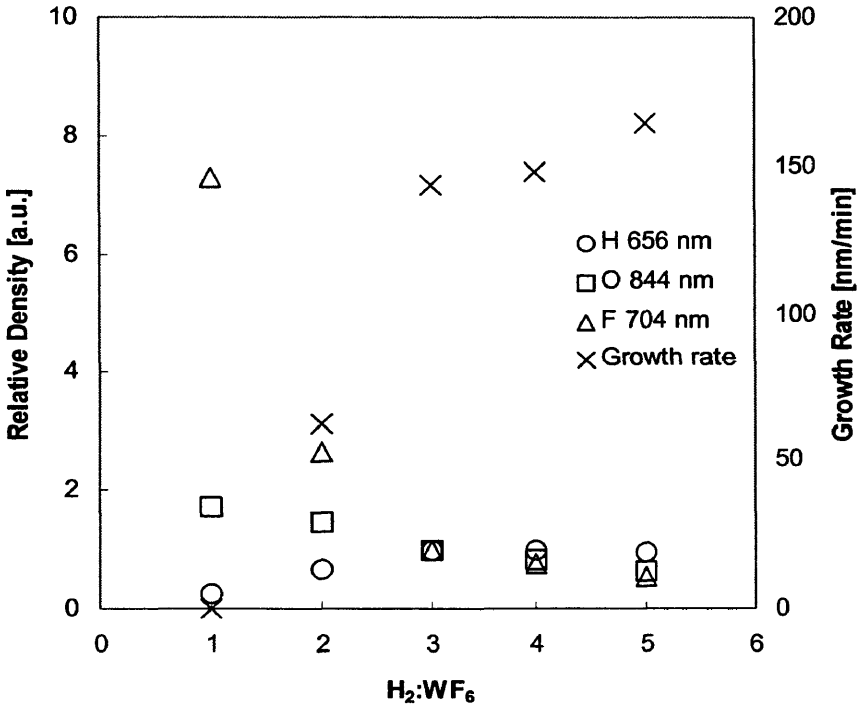

Figure 3.3: Relative atom densities and growth rate as a function of the H_2:WF_6 ratio.

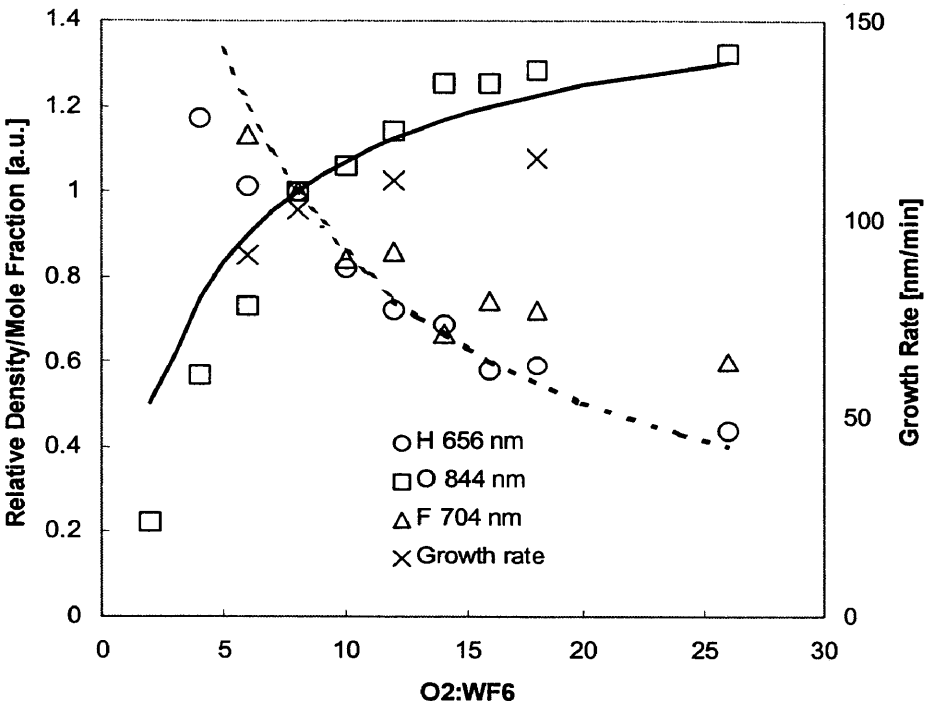

Figure 3.4: Relative atom densities and growth rate as a function of the O_2:WF_6 ratio. The dashed line is the inlet mole fraction of H_2 & WF_6. The solid line is the inlet mole fraction of O_2.

Figure 3.4 shows the dependence upon the O_2:WF_6 ratio. In these experiments the H_2 and WF_6 flowrates were fixed, while the O_2 flowrate was varied. In this case the deposition rate was correlated with the atomic oxygen density. Both initially increased with the O_2:WF_6 ratio, and saturated for values of O_2:WF_6 > 15. The relative densities of both F and H decreased with increasing O_2:WF_6. This was attributed to the dilution of WF_6 and H_2 that accompanied the increased O_2 flowrate. The lines in Figure 3.4 plot the

relative mole fractions of the initial reagent composition, which were also scaled relative to the base case condition. The dashed line is for H_2 and WF_6, while the solid line is for O_2. Comparisons of the lines with the actinometry measurements indicate that in each case the atomic densities in the reactive plasma simply tracked the mole fraction of the respective parent molecules in the reactant mixture. Thus for a fixed H_2:WF_6 ratio actinometry indicated that the primary reaction pathway was simply dissociation.

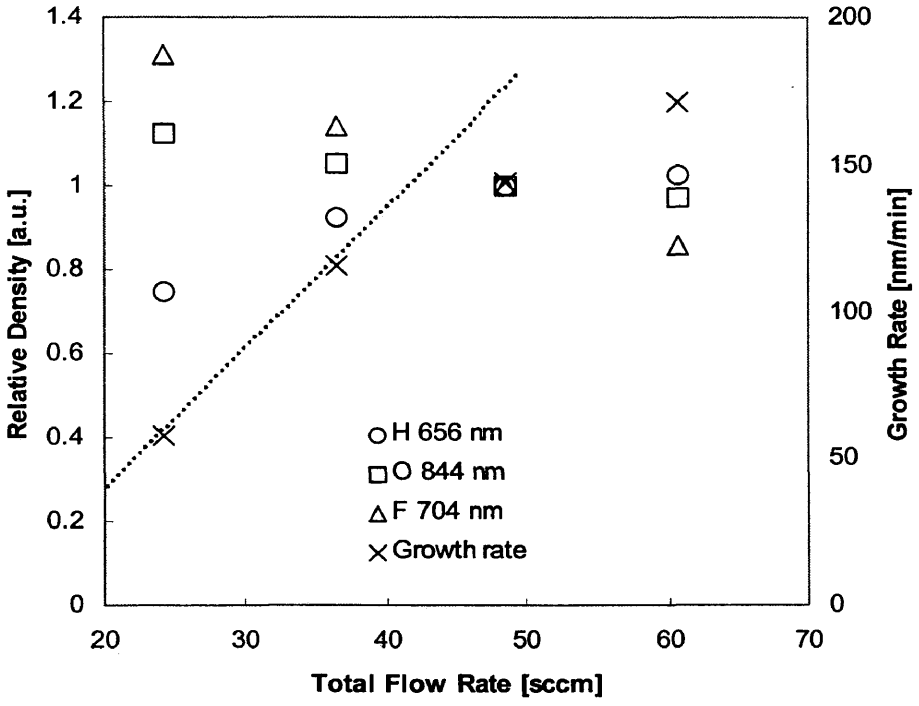

Figure 3.5: Relative atom densities and growth rate as a function of the total flow rate. Dashed line used to guide the eye.

Figure 3.5 shows the role of total flow rate on growth rate and plasma composition. In these experiments the gas composition was held constant while the total flowrate was increased. The OES signals remained relatively constant, as would be expected for a fixed composition. The growth rate increased with total flow rate. Comparison with the dashed line indicates that the growth rate increase was somewhat sub-linear, indicating that the degree of WF_6 conversion decreased slightly at the higher flowrates. This is supported by a small decline observed in atomic fluorine and associated increase in atomic hydrogen.

In general the trends observed in this work between growth rate and reactant composition were consistent with those reported previously[16]. In both cases the deposition rates were comparable, and found to be proportional to the tungsten hexafluoride flowrate. The observed H_2:WF_6 threshold for deposition was slightly higher in our work (1 vs. 0.5), and we observed no attenuation in deposition rate at high H_2:WF_6 ratios. The rate was somewhat more sensitive to the O_2:WF_6 ratio than reported in the literature.

Figure 3.6 shows the relative densities of the atomic species with respect to power. The deposition rate scaled with power as it was increased from 50 and 100 W, and the rate began to saturate with further increases in power. Although not critical to rate, it was found that rf power had a strong influence over electrochromic performance as will be discussed below. The density of all three atomic species increased linearly with power at approximately the same rate. Higher power provided for increased dissociation among

all species, but it did not appear to preferentially dissociate one molecular species over another. In the case of operating pressure, it was found that the density of all the atomic species and rate were nearly invariant over the pressure range examined.

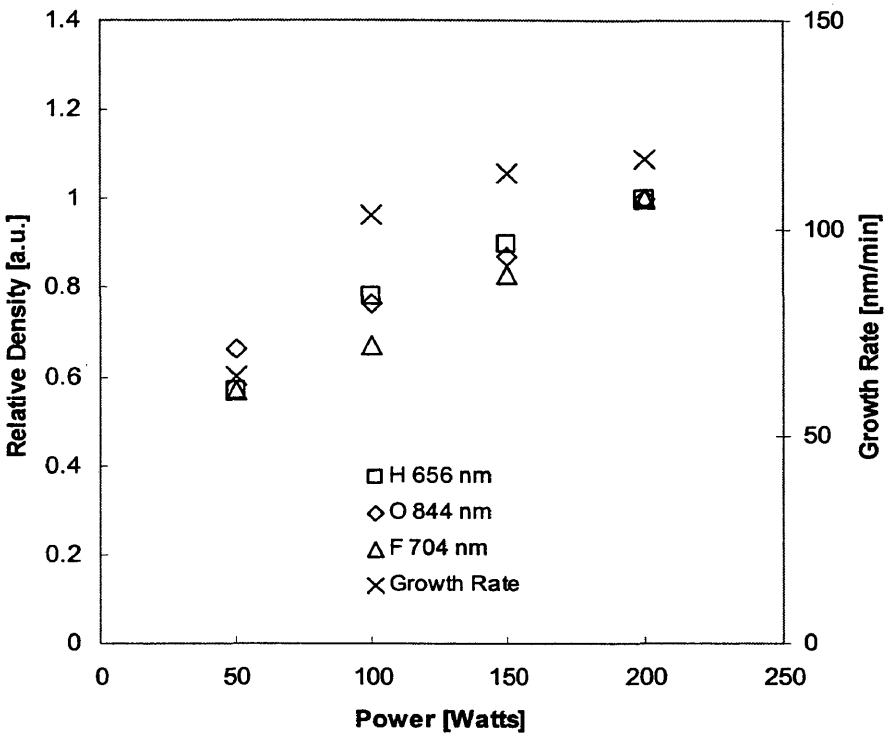

Figure 3.6: Relative atom densities and growth rate as a function of the rf power.

3.3.2 Electrochromic Performance

The electrochromic performance of the deposited films was studied using the 1M H_2SO_4 solution. Figure 3.7 shows an example of simultaneous measurement of optical

and electrochemical performance using the apparatus shown in Figure 3.2. The left axis plots the current density measured during cyclic voltammetry performed at a sweep rate of 10mV/sec. On the right axis is the corresponding transmission intensity as recorded by the photodiode. At positive bias the optical transmission was maximized. As the bias is reduced ions are transported into the film and a positive current is detected. The transmission drops concurrently until the film reaches its opaque state at the negative bias. As the bias is reversed the transmission is restored along with the departure of the ions. The asymmetry in the current curve is indicative of differences between transport and kinetics of ion insertion versus ion extraction. These CV/transmission curves were used as our electrochromic performance metric.

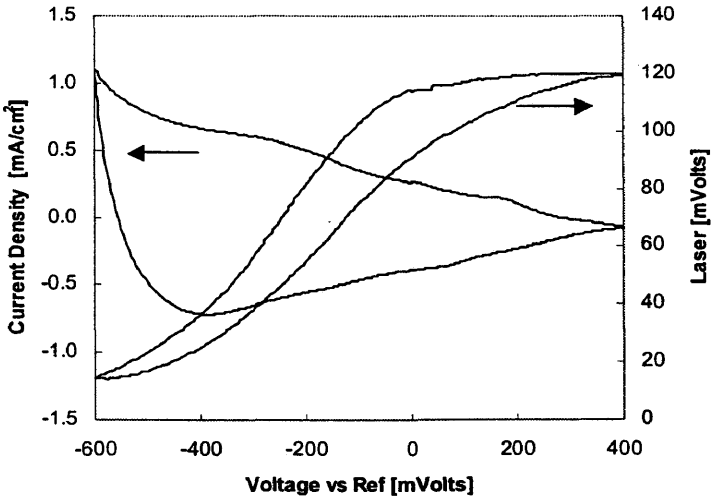

Figure 3.7: Example of a cyclic voltammetry curve and an optical transmission curve obtained at a 10 mV/sec sweep rate.

The electrochromic properties were examined as a function of the plasma operating conditions summarized in Table 3.2. Among these parameters it was found that the rf power had the most profound impact on film properties. A set of 300 nm thick films were deposited as a function of rf power at the base case plasma conditions listed in Table 3.2. Figure 3.8 shows the CVs obtained from these five films. The refractive index of each film measured at 400 nm is recorded in the legend. Figure 3.8 shows a striking correlation between power, index of refraction, and intercalated charge. The refractive index increased from 2.02 to 2.28 as the power was increased from 100 to 300 W, indicating that the film density is increasing. It is also evident from the CVs that the films grown at low power (A, B) have superior electrochromic performance. We note that for power levels below 100 W it was found that films exhibited poor adherence and poor optical quality.

It is been widely observed in other deposition systems that film density/porosity is critical to electrochromic performance[41,44]. Films require a minimum porosity to allow efficient ion intercalation. The porosity may be estimated from the following relationship:

$$Porosity(\%) = 100 \times \frac{(n_m - n_o)}{(1 - n_o)} \qquad (3.4)$$

where n_m and n_o are the measured and intrinsic refractive indices, respectively. Assuming that sample E corresponds to a dense, intrinsic tungsten oxide film, the corresponding porosity of films A and B are estimated to be 20% and 18%, respectively. At greater porosity levels film integrity is compromised as evidenced by the adhesion problems

observed below 100 W. The refractive index of PECVD-deposited films has not been previously reported, however a survey of PVD techniques[38,41,48] indicates that the refractive index can vary significantly ($1.7 < n < 2.4$) as a function of deposition conditions. The work here shows that only those films whose as-deposited refractive index is $n < 2.1$ demonstrate significant intercalation. This value of the refractive index agrees well with values obtained from similar performance measurements on tungsten oxide films deposited by magnetron sputtering[41].

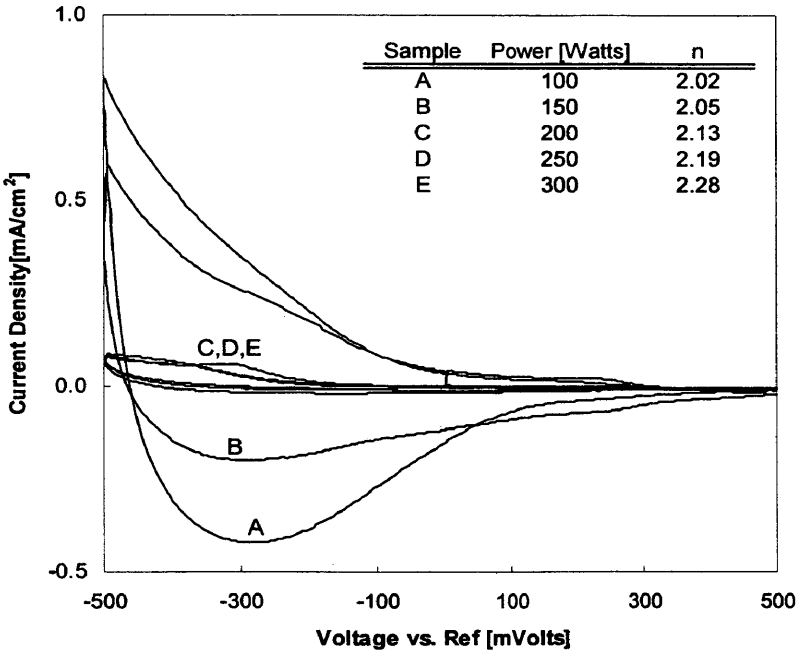

Figure 3.8: Comparison of CVs obtained from films deposited on the powered electrode as a function of rf power. Legend shows the refractive index measured at $\lambda = 400$ nm.

The dramatic variations in film density/electrochromic performance were attributed to ion bombardment. A shown in Figure 3.6, rf power has only a minor impact on rate and the neutral plasma composition, particularly for power levels > 100 W. However it is well-known that both the ion density and sheath voltage scale with the square root of plasma power[14]. Further experimental support implicating ion bombardment comes from a comparison of films deposited simultaneously on the grounded and powered electrode, respectively. All films discussed to this point were deposited on the powered electrode. The PECVD reactor used in this work is an asymmetric discharge. The ratio of the grounded electrode area to the powered electrode area is $A_G/A_P \sim 2$. The sheath voltage that accelerates ions across the respective electrode sheaths scales according to the familiar power law relation:

$$\frac{V_P}{V_G} = \left(\frac{A_G}{A_P}\right)^m \tag{3.5}$$

where the Child Sheath law predicts an exponent of $m = 4$, while experimental observations place the value closer to $m \sim 2.5$.[23] Using this relationship it is estimated that the energy of ions impinging the substrate is about 6X greater at the powered electrode. The ion flux at each electrode should be similar, controlled by the Bohm criterion in each case.

Figure 3.9 compares the properties of films grown simultaneously on the two electrodes at an rf power level of 200W. The films have dramatically different refractive indices and electrochromic response. The film deposited on the grounded electrode was

less dense as measured by the refractive index (1.93 vs. 2.13), which again translated to greater intercalation rates. It is significant to note that the deposition rates were nominally identical on each electrode. Figures 3.8 and 3.9 indicate that both ion density and ion energy contribute significantly to film density and must be carefully controlled to optimize electrochromic performance. In general we conclude that ion bombardment is detrimental to film porosity and electrochromic performance.

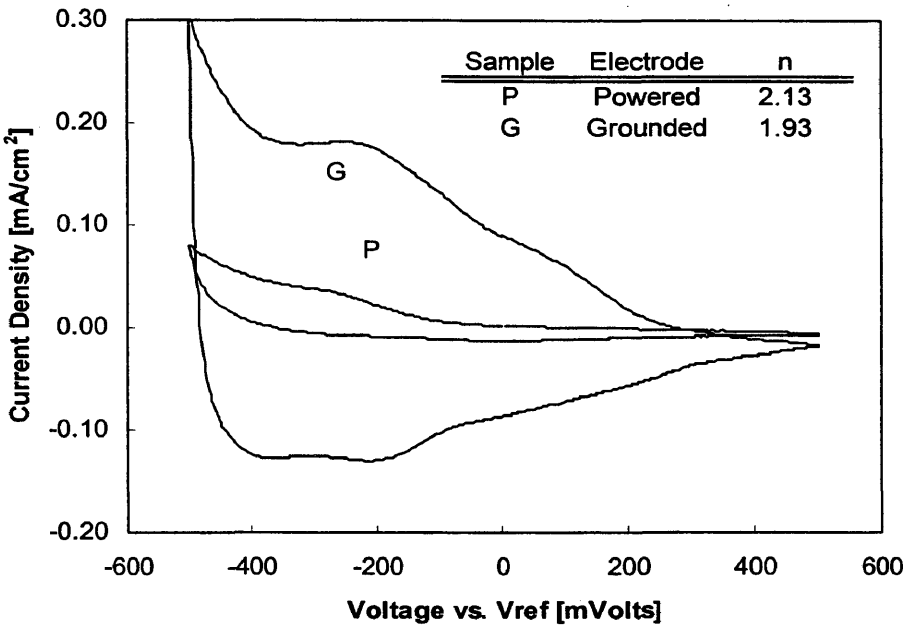

Figure 3.9: Comparison of CVs obtained from films deposited simultaneously at 200 W on the grounded and powered electrode. Legend shows the refractive index measured at $\lambda = 400$ nm.

Interestingly the influence of ion bombardment was not discussed in previous PECVD studies, which were performed at fixed power levels in a barrel reactor[15] and a parallel plate configuration[16]. Ion bombardment would be expected to be significant in both systems. It was noted that the film morphology varied widely within the barrel reactor depending on substrate location, which might have reflected variations in ion bombardment. Ion bombardment can also be important in sputtering arrangements, and indeed recent work has shown that tungsten oxide structural and optical properties are extremely sensitive to substrate biasing in these systems[49].

Finally the optimization of film thickness is presented to illustrate the value of measuring electrochemical and optical performance in registry. The optical performance depends on both intrinsic film properties as well as the film thickness. A set of five films was deposited at identical process conditions, and the thickness was varied from 200 to 1000 nm by adjusting the deposition time. It was found that refractive index, and presumably other intrinsic properties, was independent of film thickness. Figure 3.10 compares the optical transmission curves extracted from CV sweeps for each of the 5 samples. As expected, the transmission in the clear state was greatest for the thinnest films. In addition, the absorption in the opaque state also increased with film thickness. It was found that the 600 nm thick film represented the optimal thickness with respect to contrast ratio for this process condition. Its transmission in the clear state rivaled the thinnest films, while it was also nearly as opaque as the thicker films upon intercalation.

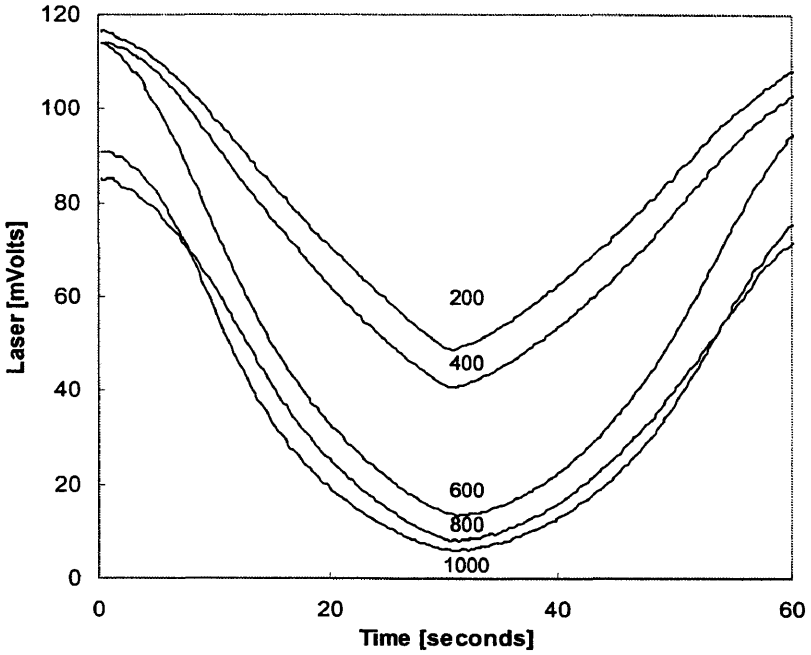

Figure 3.10: Optical transmission curves extracted from CV experiments for 5 films of varying thickness from 200 nm to 1000 nm.

3.4 Conclusions

A comprehensive investigation of plasma chemistry, film properties and electrochromic performance was presented for tungsten oxide PECVD. The effects of gas composition, total flowrate, pressure, and power were examined. In general the relative density of atomic species was found to be proportional to the initial reactant composition, indicating that dissociation is the dominant the plasma reaction pathway. For a given tungsten hexafluoride flowrate maximum deposition rates were achieved when both oxygen and hydrogen were supplied in excess. The optical and electrochemical

performance of the deposited films were examined in registry using cyclic voltammetry. Among the plasma processing parameters it was found that the rf power had the most significant impact on electrochromic performance. Experiments as a function of power and electrode selection demonstrated the significant role of ion bombardment in controlling film density. Only those films with a refractive index at 400 nm of $n < 2.1$ demonstrated efficient ion intercalation. Finally, a film thickness of ~600 nm was found to be the optimal with respect to contrast ratio.

ACKNOWLEDGEMENTS

The authors acknowledge financial support from the National Science Foundation through Award No. CTS-0093611.

CHAPTER 4

CHARACTERIZATION OF ION DIFFUSION AND TRANSIENT ELECTROCHROMIC PERFORMANCE IN PECVD GROWN TUNGSTEN OXIDE THIN FILMS

The following is a reproduction of a paper that was accepted for publication in Solar Energy Materials and Solar Cells on February 3, 2004. This chapter is reproduced as submitted except that section numbers, references, and figures were changed to conform to the thesis format.

Michael Seman, Colin A. Wolden
Chemical Engineering Department, Colorado School of Mines, Golden, CO 80401, USA

Abstract

Electrochromic tungsten oxide thin films were synthesized by plasma-enhanced chemical vapor deposition (PECVD). Film density and electrochromic performance were controlled by the degree of ion bombardment. A moderate degree of ion bombardment was optimal, and the refractive index was shown to be a sensitive indicator of electrochromic performance. Chronoamperometry in concert with optical transmission was used to determine diffusion and absorption coefficients using both H^+ and Li^+ containing electrolytes. The absorption coefficients were similar for both ions, scaling with the degree of intercalation to 50,000 cm^{-1} in the opaque state. The diffusion coefficients for optimized films were found to be relatively insensitive to the degree of

ion intercalation, with values of $\sim 10^{-9}$ and $\sim 10^{-10}$ cm^2/s for H^+ and Li^+, respectively. These values are about an order of magnitude greater than values reported for vacuum-deposited films, which was attributed to low relative density in the PECVD films. The diffusion and absorption coefficients were incorporated into a model that successfully reproduced transient optical performance.

4.1: Introduction

The electrochromic properties of transition metal oxides have been extensively studied over the past three decades [1]. Tungsten oxide is by far the most promising and widely studied electrochromic material. Thin films of tungsten oxide continue to receive attention due to numerous applications including variable transmission smart windows [42], gasochromatic sensors [40], and displays[4]. The transmission of tungsten oxides switches from transparent to opaque in response to a small applied voltage. The reversible coloration process is based on the double injection of light ions and electrons to form the tungsten bronze M_xWO_3.

$$WO_3 + xM^+ + xe^- \leftrightarrow M_xWO_3 \qquad (4.1)$$

For solid-state smart window applications Li^+ is the ion of choice due to its long-term stability. In the case of sensors, WO_3 is of particular interest due to the non-reactive nature of the induced optical response in the presence of hydrogen. In both applications it is critical to understand the dynamics of this reaction and the associated optical response.

Several mechanisms have been suggested as the limiting step in the formation of the tungsten bronze [27]

- a barrier to the ion injection at the WO_3/electrolyte interface[29-31]
- diffusion of ions within the electrochromic film [31-33]
- the series resistance of the cell [26,28]

While debate still exists, it is generally agreed that ion diffusion limits dynamics for most films. Typically chronopotentiometric and chronoamperometric techniques have been used in conjunction with transport models to extract diffusion coefficients. Reported diffusivity values range from $10^{-14} - 10^{-9}$ cm^2/s, depending on the deposition method, ionic species, intercalation level, and temperature[39]. Prevalent in the literature are comparisons between samples grown by a particular method and the resulting density, coloration efficiency, and diffusion coefficient. It has often been observed that decreasing the relative density has a dramatic effect of film performance. This was exemplified by work done by Wang et al. [50], who showed that decreasing the relative density from 0.9 to 0.75 increased the magnitude of D_{H+} by two orders of magnitude.

Thin films of tungsten oxide have been prepared through a variety of techniques; sputtering [38,40], evaporation [33,44], chemical vapor deposition[10] (CVD), sol-gel [12,27], and electrodeposition [13] have all been used. Physical vapor deposition (PVD) techniques such as sputtering and evaporation are most commonly employed for WO_3 thin film synthesis. In comparison, plasma-enhanced CVD (PECVD) has received relatively little attention. PECVD offers high deposition rates at room temperature and requires only moderate

vacuum. PECVD of tungsten oxide films was first demonstrated by Tracy and Benson[15] in 1986. More recently, Henley and Sacks[16] qualitatively described plasma composition, deposition rate, and film properties. However, to date there has been limited quantitative evaluation of ion diffusion or electrochromic performance for PECVD material. In previous work [51], we showed that ion bombardment had a profound impact on film density and electrochromic performance. In this work we evaluate the diffusion and absorption coefficient of PECVD WO_3 using both Li^+ and H^+ containing electrolytes. The diffusion and absorption coefficients were evaluated as a function of ion intercalation. A model incorporating these values was developed, and used to successfully predict transient optical performance.

4.2 Experimental

Deposition of tungsten oxide was performed in an asymmetric, capacitively-coupled plasma chamber. Power was supplied by a 300W rf supply operating at 13.56 MHz and coupled using a matching network. Further details of this custom built chamber are provided in the literature[17]. Silicon wafers and transparent conducting tin oxide coated glass with a sheet resistance of 11 Ω/ purchased from Libby-Owen-Ford (LOF) were used as substrates. Polished silicon served as an ideal substrate for film thickness and refractive index measurements, while the LOF glass substrates were used to evaluate electrochromic performance.

All depositions were done at ambient temperature using mixtures of tungsten hexafluoride, oxygen, and hydrogen. Previous work investigated the role of reactant composition and plasma operating conditions. It was found that ion bombardment had the most significant impact on film performance. Film properties were also relatively insensitive to pressure or composition as long as the H_2:WF_6 and O_2:WF_6 ratios were sufficiently high [51]. In this work these variables were held constant at P = 200 mTorr, H_2:WF_6 = 4, and O_2:WF_6 = 17. The degree of ion bombardment was controlled by the power and choice of electrode. In our asymmetric configuration, the ratio of grounded to powered electrode area was ~2:1. In accordance to the well-known power law relation [14], the sheath voltage across the powered electrode is approximately 6 times greater than that of the grounded. In addition, the ion density is proportional to power and the sheath voltage scales with rf power to the one half power [14].

The film density was inferred from measurements of the refractive index. Spectroscopic ellipsometry was performed using a J.A. Woollam ellipsometer and analyzed with the associated WVASE32 software. Films were measured over a range of 400-1200 nm at 70° angle of incidence. The wavelength-dependent optical constants were fitted using a Cauchy model, which has been successfully employed for tungsten oxide films[38].

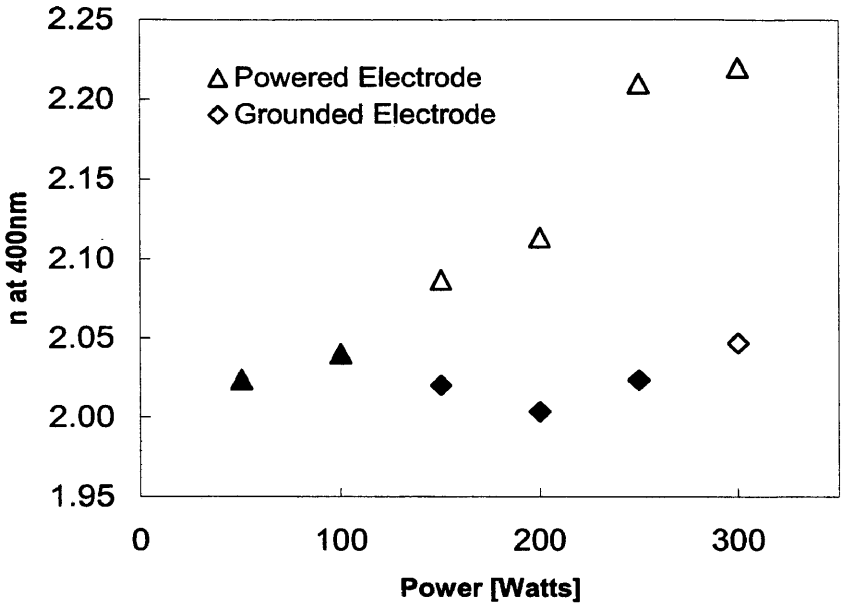

Figure 4.1: The refractive index as a function of rf power for films grown on the grounded and powered electrodes. Solid symbols indicate films that displayed fast electrochromic response.

Figure 4.1 shows the index of refraction recorded at 400 nm for samples grown on both electrodes as a function of rf power. Solid symbols in Figure 4.1 indicate films that displayed rapid, reversible electrochromic performance. In contrast, open symbols had either poor or irreversible performance. The refractive index increased sharply with power for films deposited on the powered electrode, while a much weaker dependence was observed for substrates placed on the grounded electrode. However, we also note that films deposited on the grounded electrode at power levels <150 watts were often hazy or

poorly adhered. Since neither optical nor electrochemical properties could be measured reliably, these films were excluded from Figure 4.1. Films whose refractive index was >2.05 did not display efficient ion intercalation. The films that did had a narrow range of indices, $2.00 < n < 2.05$, there was little variability in performance. The data presented below is from a film deposited at 150 watts on the grounded electrode. However, the films with filled in symbols all had very similar performance. Optimized films require some degree of ion bombardment. The combination of either low power on the powered electrode or moderate power on the grounded electrode produced working films. The refractive index was observed to be a very sensitive predictor of performance.

Film performance was characterized using a custom built apparatus capable of simultaneous analysis of optical and electrochemical performance. Many groups [26,44] have employed similar approaches to evaluate tungsten oxide. Deposited films were suspended in an electrolyte solution of either 1 M H_2SO_4 or 1 M lithium perchlorate in propolyene carbonate. Potentiostatic chronoamperometry experiments were performed using a Gamry model PC4 Potentiostat in the conventional three-electrode configuration. The working electrode was contacted to the LOF substrate, a graphite rod served as the counter electrode, and all measurements were referenced against a saturated calomel electrode. A HeNe laser operating at 633 nm was directed at normal incidence through the electrochromic film, and the transmitted intensity was evaluated using a Thorlabs DET110 photodiode. The photodiode was calibrated using *ex-situ* measurements of absolute transmission using a Cary 5G UV-Vis-NIR spectrophotometer. In the

spectrophotometer the contribution of the LOF substrates was subtracted out, providing measurements indicative of the WO_3 film alone. A linear relationship was observed between absolute transmission and the photodiode signal, and this was used to evaluate optical density. Both diagnostics were interfaced through a PC so that optical and electrochemical performance were monitored in direct registry. Further details may be found in the literature [51].

4.3 Results

4.3.1 Evaluation of the Diffusion Coefficient

Numerous groups have evaluated the diffusion of light ions in WO_3 films. Experimental techniques used have included potential steps [52], cyclic voltammetry[53], and ac impedance [32]. The potentiostatic intermittent titration technique (PITT) is a version of the first technique that employs a series of successive voltage steps and measures the current response[54]. By applying sufficiently small steps, one may safely assume that the diffusion coefficient and emf are constant within a step. PITT was recently used to characterize Li^+ diffusion in other oxide thin films [37]. Similar galvanostatic and potentiostatic techniques have also been used to measure diffusion coefficients in WO_3 [13,44].

In this work, successive steps of 0.03 volts were applied to determine the diffusion coefficient as a function of intercalation for both Li^+ and H^+. When the current

decayed to less than 1% of its original value, the total integrated charge was used to solve for the ion content in the film. This value served as the saturated boundary condition at the WO_3/electrolyte interface for the current step (C_s), and as the initial value for the subsequent step (C_o). A no-flux boundary condition was applied to the LOF-WO_3 interface. Under these conditions the analytical solution to Fick's second law [36,37], and associated current response are given by:

$$C(z,t) = C_s - (C_s - C_o)\frac{4}{\pi}\sum_0^\infty \left[\frac{1}{2n+1}\sin\left(\frac{(2n+1)\pi z}{2L}\right)\exp\left(-\frac{(2n+1)^2\pi^2 Dt}{4L^2}\right)\right] \qquad (4.2)$$

$$I(t) = \frac{2nF(C_s - C_o)D}{L}\sum_0^\infty \exp\left(-\frac{(2n+1)^2\pi^2 Dt}{4L^2}\right) \qquad (4.3)$$

where $C(z, t)$ is the ion concentration, D is the diffusion coefficient, L is the thickness of the film, F is Faraday's constant, C_o and C_s the initial and saturated concentration, respectively.

The diffusion coefficient was determined by selecting the value that provided the best fit between experiment and model. Figure 4.2 shows representative examples of model fits to the current response in both electrolytes. Repeated steps yielded the diffusion coefficient as a function of intercalation level in M_xWO_3 over the range $0.02 > x > 0.20$. Figure 4.3 displays these results on a semi-log plot. The diffusion coefficient ranged from $1.3 \times 10^{-9} - 2.6 \times 10^{-10}$ for H^+, and from $1.8 \times 10^{-10} - 6.6 \times 10^{-11}$ in the case of Li^+. The symbols in Figure 4.3 represent the data, while the smoothed curves reflect an

empirical fit to $D(x)$ that is used later in transient modeling of the optical response. As seen by others, the diffusivity declines slowly with extent of intercalation [39,44,55]. In addition, the higher diffusivity of protons relative to lithium ions is also consistent with literature observations [50].

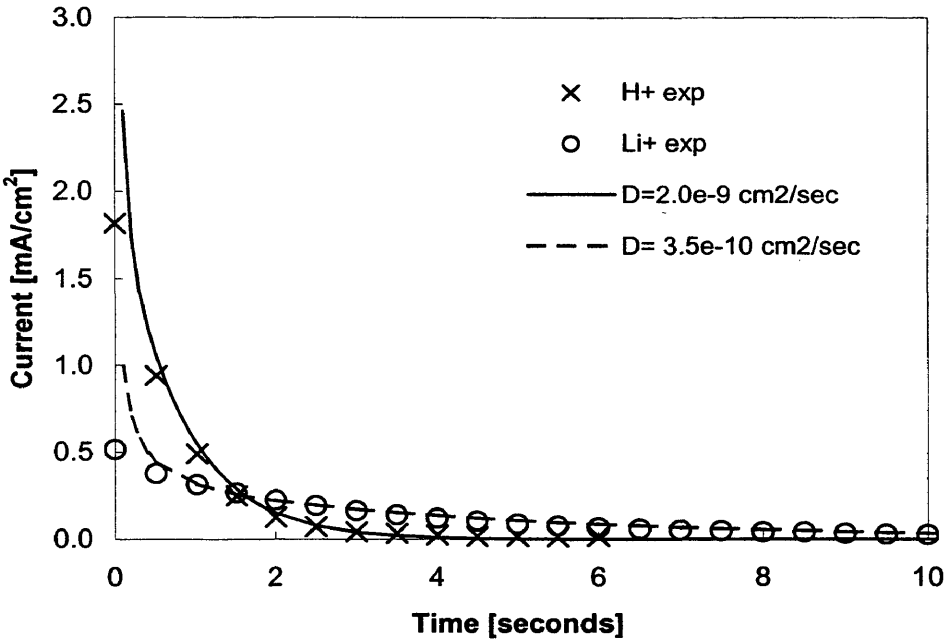

Figure 4.2: Examples of comparisons between measured (points) and modeled (lines) current response to PITT steps for H^+ and Li^+.

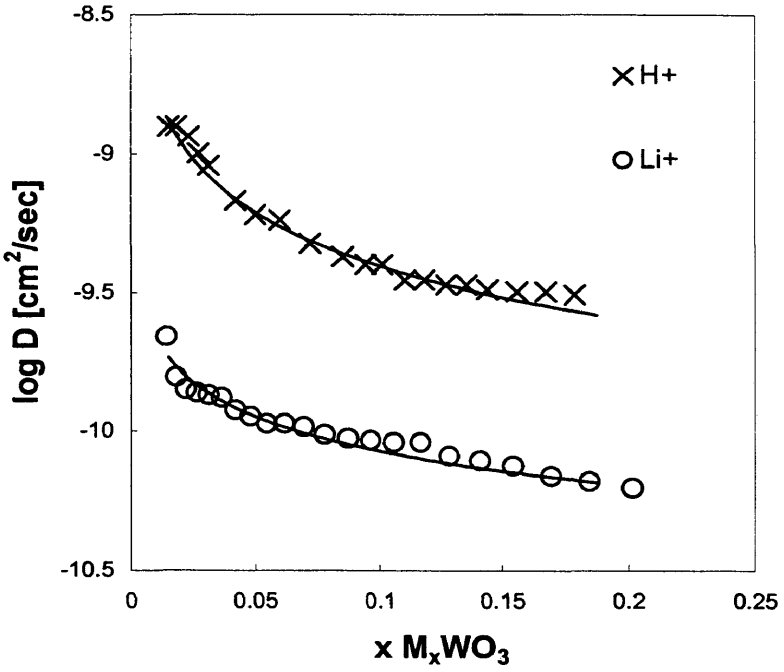

Figure 4.3: Semi-log plot of H^+ and Li^+ diffusion coefficients in WO_3 as a function of ion intercalation. Lines are empirical fits to $D(x)$ that were used to model transient optical response.

Reported diffusion coefficients for lithium range from 10^{-14} cm^2/s for bulk WO_3[56] films to 10^{-9} cm^2/s for highly porous electrodeposited films [13]. In a recent review article, Granqvist [39] summarized several studies that placed D_{Li+} for vacuum-deposited films between 5 x 10^{-13} cm^2/s and $10^{-11}cm^2/s$, scaling with the inverse of film density. In this work we found D_{Li+} to be superior to the best values found in these studies, but inferior to electrodeposited films.

For both H^+ and Li^+ the diffusion coefficients for PECVD grown WO_3 were about an order of magnitude greater than leading PVD films. This is attributed to the control of the degree of ion bombardment and thus, relative density. In their work, Shen et al. [13] reported a Li^+ diffusion coefficient of 1.2×10^{-9} cm^2/s for electrodeposited films with a density of 5.0 g/cm^3. Compared to the density of crystalline WO_3 (7.16 g/cm^3) [57] this corresponds to a relative density of 0.70. For vacuum deposited tungsten oxide films relative densities ranges from 0.74 – 0.91 [1,58]. Using a refractive index at 400 nm of 2.4 for fully dense films[39], the relative density of PECVD films that demonstrated rapid electrochromic performance ($2.0<n<2.05$) fall into the range of 0.71– 0.75. As with the diffusion coefficients, the relative density of PECVD films is bound by values obtained for electrodeposited films at the low end and leading PVD films at the high end. This clearly confirms that film density is the key factor for producing films with a quick electrochromic response. As inferred from the range of our index of refraction measurements, PECVD offers a novel means of controlling density in WO_3 films, and thus the response rate.

4.3.2 Evaluation of the Absorption Coefficient and Optical Density.

The optical absorption coefficient at 633 nm was determined using Beer's Law.

$$I = I_o \exp(-\alpha L) \tag{4.4}$$

where I_o is the initial intensity of the He-Ne laser, I the final intensity, L the thickness of the film in cm, and α the absorption coefficient in cm^{-1}. The absorption coefficient was measured in experiments similar to the PITT approach used to measure diffusion coefficients. The voltage was modulated in a series of steps and allowed to reach equilibrium. Measurements of the initial and end point laser intensity from each step were used to determine the absorption coefficient as a function of intercalation. The absorption coefficient as a function of ion content obtained from representative samples and both electrolytes is shown in Figure 4.4. The solid symbols designate the acidic electrolyte, while open symbols signify the lithium electrolyte. As seen in Figure 4.4 the absorption coefficient was insensitive to given electrolyte and initially increases linearly with degree of intercalation before attenuating for $x > 0.2$ and saturating at ~50,000 cm^{-1}. Samples 150GA and 150GB were 300 and 600 nm thick, respectively, ensuring that our measurements were truly indicative of intrinsic film properties. The curve shown in Figure 4.4 is an empirical fit that is used in the modeling described in the following section.

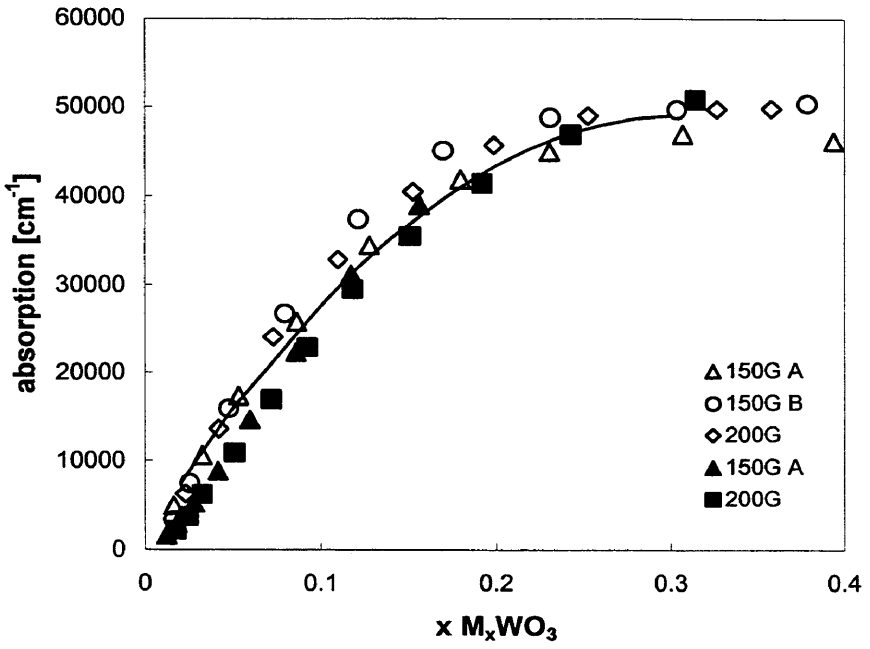

Figure 4.4: The WO_3 absorption coefficient at 633 nm as a function of ion intercalation. Solid symbols designate H^+, open symbols designate Li^+, and the line is an empirical fit to $\alpha(x)$ that was used to model transient optical response.

Changes in optical density (Δ O.D.) are more commonly reported in the literature. The ΔO.D. is an extrinsic film property that depends on film thickness and is defined as[9]

$$\Delta O.D. = \log\left(\frac{T_o}{T}\right) \tag{4.5}$$

where T_o and T represent the initial and final transmission, respectively. Figure 4.5 shows the measured change in optical density as a function of intercalation for two representative films of 300 and 600 nm thickness. Previously we found that 600 nm was an optimal thickness for maximizing the modulation difference between bleached and

colored states [51]. For reference, a Δ.O.D. of ~1.0 corresponds to absolute transmission values of 95% and 10% for the bleached and colored states, respectively. In the following section the validity of experimentally measured diffusion and absorption coefficients were tested by examining their utility in predicting transient optical performance in response to large voltage steps.

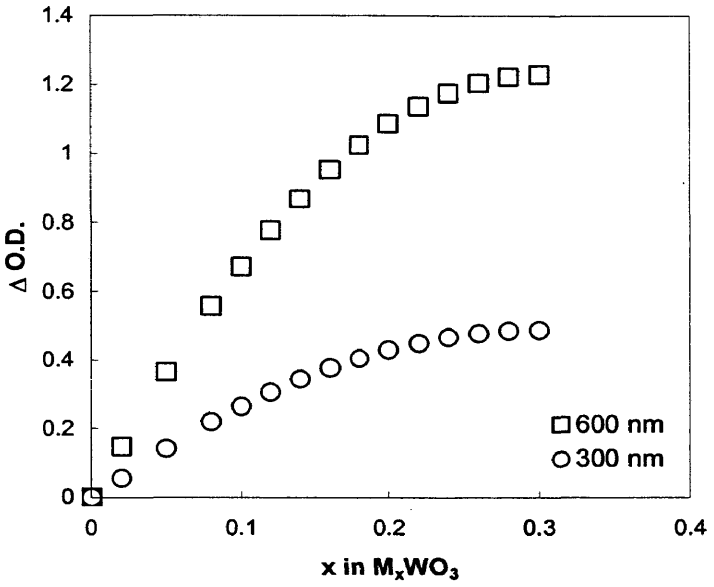

Figure 4.5: The change in optical density as a function of ion intercalation for films of different thickness.

4.3.3 Transient Optical Performance

A model was developed to simulate the transient optical response of PECVD tungsten oxide to large potential steps. This complicates the solution to Fick's law in two important ways. First, the diffusion coefficient is not constant, and the empirical

functions for $D(x)$ represented by the curves in Figure 4.3 were used. Second, as intercalation proceeds, an *emf* appears across the WO_3-electrolyte interface that opposes current flow. Several authors [28,33,44] have incorporated the effect of *emf* into their analysis of ion diffusion by making the following changes. First the coloration voltage, which is the driving force for intercalation, is set to the applied voltage minus *emf*:

$$V_c(t) = V_a - emf(x) \tag{4.6}$$

Second, the ion flux at the WO_3/electrolyte interface is controlled by Ohm's law, and the boundary condition to Fick's second law must be modified to the following

$$nFD\frac{\partial C}{\partial z}\bigg|_{z=0} = \frac{V_a - emf(x)}{R_s} \tag{4.7}$$

where R_s is the specific series resistance [Ω-cm^2].

Incorporation of the boundary condition expressed in Eqn. 4.7 requires that the series resistance and the concentration-dependent *emf*(x) must be known. The value of *emf* as a function of ion intercalation was measured by galvanostatically sourcing the current and measuring the potential. Figure 6 plots the value of *emf* vs. the saturated calomel reference for both electrolyte solutions. At low levels of intercalation the *emf* is slightly positive, as ion intercalation precedes the *emf* quickly declines to negative potentials. These *emf* measurements were fit to the following commonly used equation [33]:

$$emf(x) = a + bx + v\frac{RT}{F}\ln\left(\frac{x}{1-x}\right) \tag{4.8}$$

where R is the universal gas constant and a, b, and v are constants that in principle can be deduced from thermodynamic[59] and kinetic [31] considerations, but here serve only as fitting parameters. The *emf* fitting parameters obtained for both electrolytes were very similar to those reported in the literature [33]. Next the specific series resistance (R_s) was determined by plotting the current density measured versus applied voltage at short times, when the response is indicative of the experimental setup and not ion diffusion [33]. The current density measured at t = 0.25 s is plotted versus the applied potential in Figure 4.7. At this short time an ohmic relationship is clearly observed, and the series resistance was obtained from the slopes. Values of 30 and 270 Ωcm^2 were found for H^+ and Li^+ electrolytes, respectively. Again, these values are very comparable to literature reports for both electrolytes [25,33].

The use of the new boundary condition and a concentration-dependent diffusion coefficient require a numerical solution to Fick's second law. An explicit finite difference model was used to determine the resulting concentration profiles $C(z, t)$ in response to large voltage steps. At each time step an effective absorption coefficient, $\alpha_{eff}(t)$, was obtained by integrating the empirical relation for $\alpha(x)$ shown in Figure 4 over the concentration profile. The transient laser intensity was then evaluated using Beer's law, and converted to ΔO.D. using Eqn. 4.5.

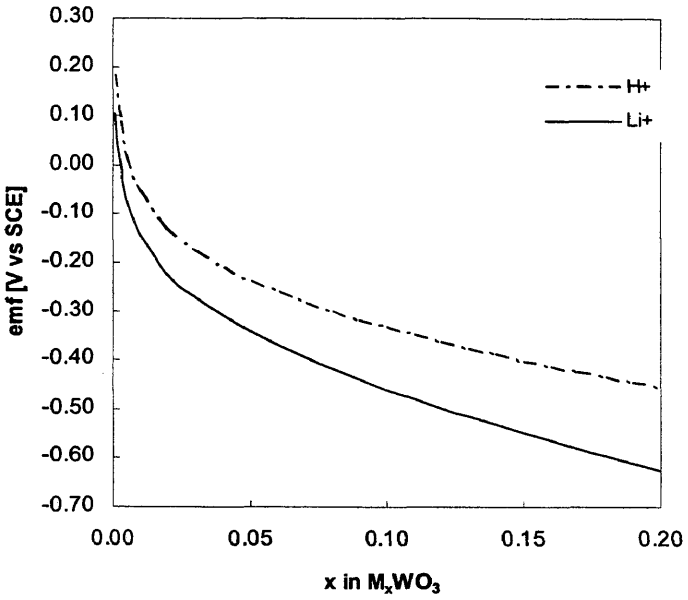

Figure 4.6: The *emf* as a function of ion intercalation for both electrolytes.

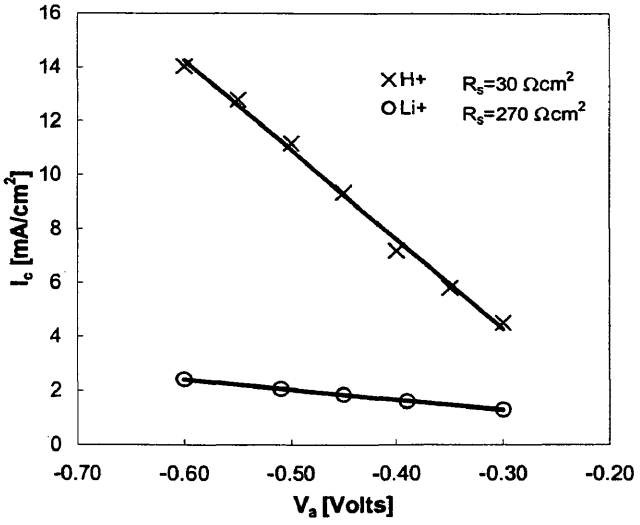

Figure 4.7: The current density measured at t= 0.25 seconds vs. applied potential for both electrolytes. Specific series resistance values were determined from the slopes.

Figure 4.8 compares experimentally measured response in optical density to potential steps with model predictions for both electrolytes. Very good agreement was observed for both electrolytes. The applied voltage sets the saturation level of the curves shown in Figure 4.8. When the *emf(x)* reaches the applied voltage, the flux of ions entering the film goes to zero as expressed in Eqns. 4.6 and 4.7. The *rate* at which a film approaches saturation is controlled by the diffusion coefficient. The impact of diffusivity is shown more explicitly in Figure 4.9, which compares Li^+ and H^+ electrolytes directly. In this case a 600 nm film was subjected to –0.6 V and –0.4 V steps for Li^+ and H^+ electrolytes, respectively, so that the saturation composition and ΔO.D. would be essentially the same (see Fig. 4.6). The response time in the aqueous solution was about ten times faster than lithium, reflecting the difference in diffusivity. To further illustrate this point the dashed line in Fig. 4.9 is a model prediction assuming a constant diffusivity value of 10^{-11} cm^2/s, which is characteristic of lithium diffusion in PVD films. The PECVD material clearly has a much more rapid response. Overall, the excellent agreement displayed in Figs. 4.8 and 4.9 validate our measurements of diffusion and absorption coefficients.

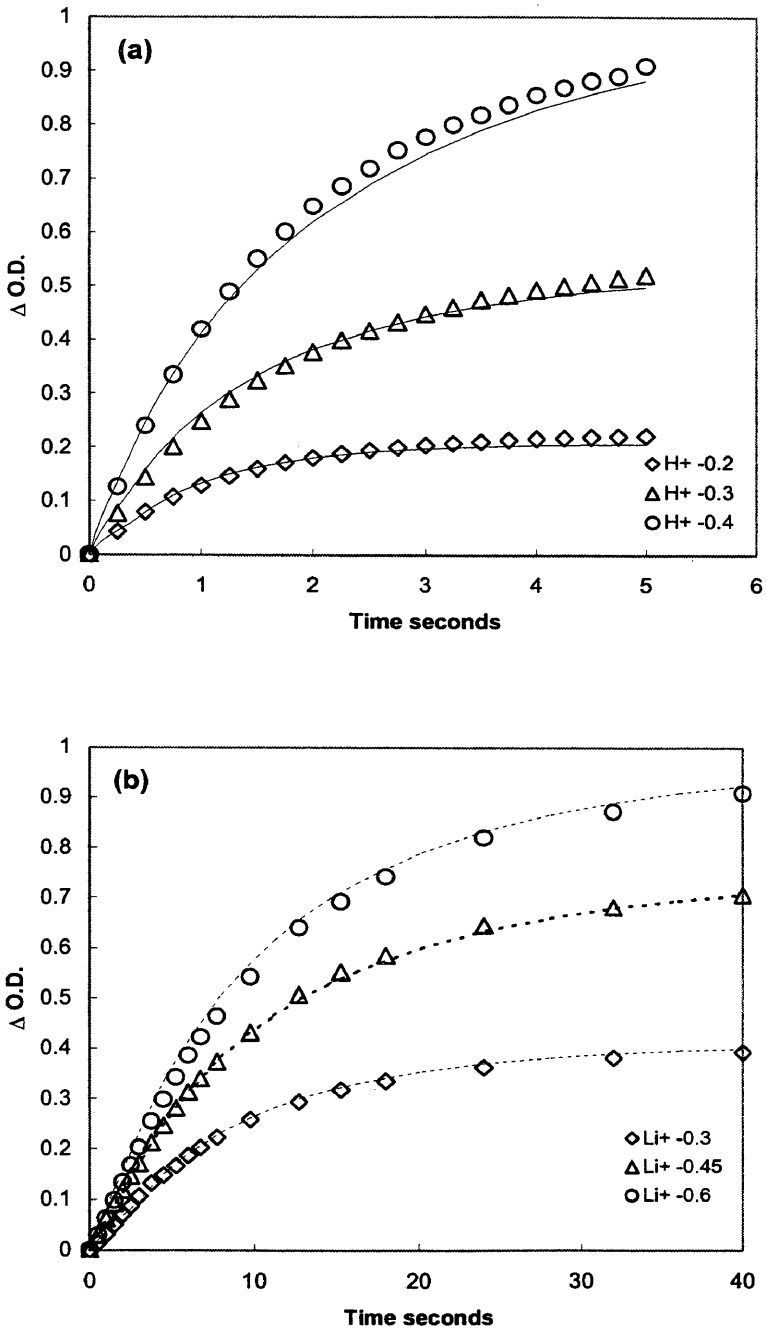

Figure 4.8: Comparison between model and data for the optical response for several different voltage steps. (a) H^+ electrolyte (b) Li^+ electrolyte

4.4 Conclusions

PECVD offers an attractive route for high rate synthesis of tungsten oxide thin films. Film density and electrochromic performance may be tailored through appropriate control of ion bombardment. The refractive index provides a convenient measure of density, and is an accurate predictor of electrochromic performance. Chronoamperometry in concert with optical transmission were used to evaluate diffusion and absorption coefficients as a function of the degree of ion intercalation for both hydrogen and lithium. Diffusion coefficients for optimized PECVD films were found to be an order of magnitude greater than values from films deposited by conventional PVD techniques. A model was developed to predict optical performance that incorporated experimentally measured diffusion and absorption coefficients. The model successfully predicted the transient optical response to large potential steps. This demonstrates that is PECVD is a promising technique for the synthesis of high performance tungsten oxide thin films.

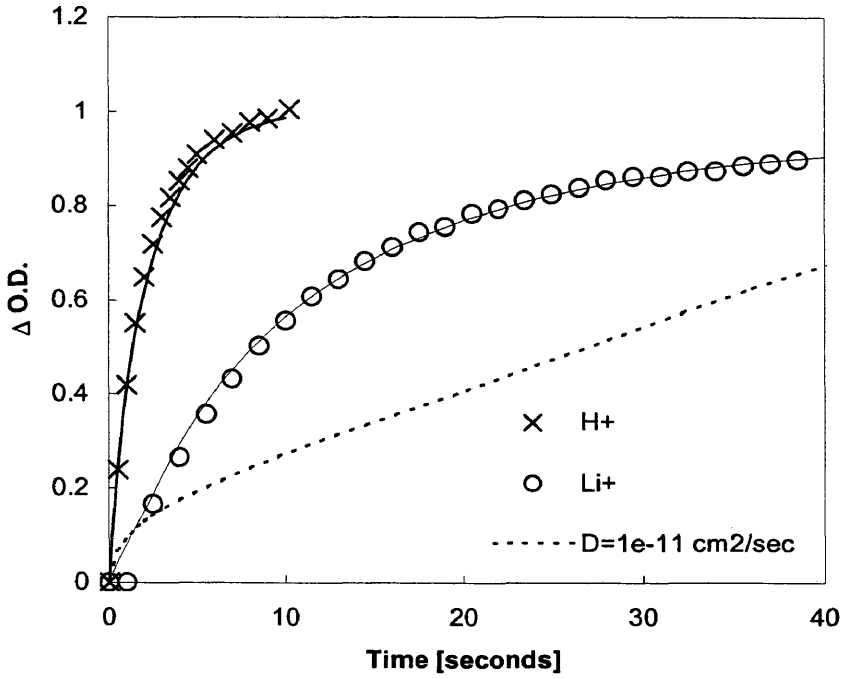

Figure 4.9: Comparison between the measured (points) and modeled (lines) transient response of optical density to large step voltages for both electrolytes. Also shown is a model prediction (dash line) of the response in lithium assuming a constant diffusivity of 10^{-11} cm^2/s.

CHAPTER 5

COMPLETE DEVICES AND RECOMMENDATIONS

Typically, an electrochromic device consists of five layers that in principle could be deposited by PECVD. The central layer is an electrolyte for light ions, typically H^+ or Li^+. This ion conductor is sandwiched between the optically functional electrochromic layer on one side, and the ion storage layer that serves as a counter electrode on the other side. Optical modulation is achieved when ions are moved back and forth between the electrochromic layer and the counter electrode. The shuttling of ions is induced by a static electric field applied between two transparent conducting oxides on the outside of the electrochromic and ion storage layers. Essentially an electrochromic device is a battery in which the charged state manifests itself as an optical effect[39].

The overall pairing of the specific materials is as important to the performance characteristics of a complete device as the individual film properties. In general, the coloration current for a complete device may be expressed as[60]

$$I_c = \frac{V_e}{R_t} = \frac{[V_a - (emf_{IS} - emf_{EC}) - V_b]}{R_t} \qquad (5.1)$$

where V_e is the effective coloring voltage, V_a is the applied voltage, V_b is the sum of all interface barriers, R_t is the sum of all the resistances to ionic current in the various layers, and emf_{IS} minus emf_{EC} is the difference in electromotive force between the ion storage

and electrochromic layer. Device switching time and performance is proportional to coloration current and thus dependent on material selection. Equation 5.1 indicates that ideally the storage and electrochromic layers have similar *emf* values. It has been shown that their difference is the primary factor in setting the applied voltage[61]. This is particularly crucial for applications that aim to use low voltage solar cells to provide the voltage to switch the device[60]. The barrier voltage, V_b may be minimized by decreasing interface defects. Finally to minimize R_t, the ion conductivity must be maximized in all layers. Of course, film thickness should also be minimized with respect to R_t, however optical performance often sets film thickness requirements.

The long-term goal of this project is to deposit a complete electrochromic device through PECVD. Previous theses[20,62] in our group focused on the deposition of conducting oxides that could serve as the contacts in an electrochromic device. The following section reviews literature regarding leading candidates for the ion storage and ion conducting layers required in a complete electrochromic device. The implementation issues for depositing these materials by PECVD are discussed.

5.1 Ion storage layer

5.1.1 Requirements and Characterization

Requirements for the ion storage layer are very similar to those of the electrochromic layer, and this film may be characterized with similar electrochemical and

optical techniques. It is desirable for architectural applications that complete devices be neutral gray in the colored state. Tungsten oxide, the de facto electrochromic layer, possesses a deep blue colored state. Consequently, a storage layer with an absorption spectra complementary to that of tungsten oxide to produce overall color neutrality is favorable. In addition, maximizing the broadband transmission in the clear state on the complete device is crucial. Vanadium and nickel oxide are the two leading candidates for the ion storage layer that share complimentary changes in free energy upon ion extraction to that of WO_3, enabling reasonable switching voltages. Therefore, both of these materials have been incorporated in numerous different electrochromic devices configurations[39,63].

5.1.2 Vanadium oxide

Thin films of V_2O_5 have been deposited through rf sputtering[64,65], thermal evaporation[60,66], pulsed laser deposition[37](PLD), sol-gel[67], and PECVD[68,69] techniques. There has also been strong interest in vanadium oxide thin films for lithium batteries because of their large ion storage capacity[37,64,68]. However, the optical properties of V_2O_5 are a concern since V_2O_5 films are incapable of attaining a fully transparent state[63,70]. Films of V_2O_5 darken upon lithium extraction in the blue and near UV which is beneficial, but they have weak coloration upon lithium insertion in the red and near infrared. This weak coloration limits the visible transmission under increasing levels of intercalation.

Several authors suggest that the issues with clear state transmission can be overcome through appropriate preparation of the V_2O_5 layer. Stuart et al.[71] suggest that V_2O_5 may still serve as a suitable storage layer if intercalation in the clear state is limited and an appropriate thickness is chosen. A yellow to colorless transition was observed for films around 120 nm thick on 10-15 mC/cm^2 of lithium insertion. Ozer et al.[67] used sol-gel techniques to dope vanadium pentoxide with titanium to produce films of $(TiO_2)_x(V_2O_5)_{1-x}$ with titania mole fractions ranging between 5 and 20%. The authors found that 5 mole percent doping produced an optimized clear state transmission over non-doped vanadium oxide films.

Despite less than perfect optical properties, V_2O_5 is commonly employed as the cathode in Li based electrochromic devices[60,72-74]. Furthermore, in regard to PECVD, thin films of V_2O_5 have already been successfully deposited and studied as cathodes for thin film batteries. Zhang et al.[68] deposited vanadium oxide films using vanadium oxytrichloride ($VOCl_3$), O_2 and H_2 as precursors. Similar to the tungsten oxide system the hydrogen is added to accelerate the forward reaction and scavenge chlorine.

$$4VOCl_3 + 6H_2 + 3O_2 \leftrightarrow 2V_2O_5 + 12HCl \qquad (5.2)$$

$$12VOCl_3 + 18H_2 + 7O_2 \leftrightarrow 2V_6O_{13} + 36HCl \qquad (5.3)$$

Depositions were carried out between room temperature and 300°C in a parallel plate capacitively-coupled plasma chamber. All films up to 300°C were found to be amorphous. The authors showed that the oxygen flow rate could be optimized to produce vanadium oxide stoichometries best suited for battery applications. With similar

motivations, Barreca et al.[69] deposited V_2O_5 from the organometallic precursor, $VO(Hhfa)_2H2O$ (HhFa = 1,1,1,5,5,5=hexaflouro-2,4-pentanedione). However, this precursor is not commercially available.

Films of V_2O_5 can reach intercalation extents greater than one. Murphy and Christian[75] reported a Li to V_6O_{13} ratio of eight, however typically values of slightly greater than one are reported. Comparatively, this work found opaque state transmission of WO_3 to saturate at a molar ratio of ~0.15. The high ion storage capacity of vanadium oxide may be beneficial to electrochromic applications in that a very thin layer could be used to minimize absorption issues. A thin vanadium oxide film may provide the equivalent charge required by the thicker WO_3 layer, while still remaining thin enough to reduce the residual absorption in the clear state. Thin layers are also beneficial to the overall cell resistance.

5.1.3 Nickel Oxide

Another transition metal oxide for application as the ion storage layer is nickel oxide. Nickel oxide has been deposited through a variety of techniques including evaporation[76], sputtering[77,78], electrodeposition[79], sol-gel[80], and PECVD[81]. In general, it was found that chemical and electrochemical techniques lead to highly porous films with quick response times, but with degradation effects arising around 10^3 cycles[82]. While there has been extensive characterization of NiO derived from PVD techniques[83-85], sol-

gel[80], and electrodeposition[86], there has been no evaluation or optimization of PECVD-derived NiO for electrochromic applications.

NiO is a prime candidate for application as a storage layer mainly due to its favorable optical properties. Fully functional solid-state devices[87,88] pairing NiO with WO_3 have shown a larger transmission modulation compared with similar devices[63,72] incorporating V_2O_5 and WO_3 films. However, similar to vanadium oxide, NiO also has some residual optical absorption in the $400 < \lambda < 500$ nm wavelength interval[63] in its bleached state. To mitigate this, films may be doped with either aluminum or magnesium. In recent work carried out by Granqvist et al.[63] films of $NiAl_{0.56}O_{2.26}$ and $NiMg_{0.8}O_{2.4}$ prepared through magnetron sputtering of Ni, Mg, $NiAl_{0.56}$ in Ar/O_2 or $Ar/O_2/H_2$ were found to have a decreased absorption in the above mentioned wavelength interval and displayed a visual appearance towards a more color-neutral state.

In rf sputtering of pure nickel targets in an oxygen plus argon atmosphere NiO films obtained by Faria et al.[77], the transmission varied by 20% depending on the process conditions. Films with the maximum as-deposited transmission also displayed the highest change in optical density and had the highest porosity. This is analogous to the results presented in this work related to the performance of WO_3. However, unlike electrochromic WO_3 the coloration mechanism in NiO is not well understood. Therefore, it is not known if the increase in porosity benefits electrochromic performance through increased bulk ion conductivity or increased surface contact area for surface reactions between electrolyte and film.

When referring to nickel oxide in the literature, the term "nickel oxide" is often used in the general sense to include not only NiO, but also the oxide's hydrous forms as well. The electrochromic proton based coloration reaction has been suggested to be the following:

$$\underset{\text{bleached}}{Ni(OH)_2} \leftrightarrow \underset{\text{colored}}{NiOOH} + H^+ + e^- \qquad (5.4)$$

Wruck and Rubin[84] performed x-ray diffraction and IR absorption measurements on bulk films of both NiO and $Ni(OH)_2$ and found no changes in crystal structure upon oxidation or reduction of the films. Optical changes in NiO are induced by only a small charge transfer of about 20 mC/cm^2. This in conjunction with the previous electrochemical experiments on both NiO and $Ni(OH)_2$ is indicative of electrochromic reactions only taking place at hydroxylated surface sites. However, in lithium based ion batteries the intercalation dynamics of NiO was also studied and a completely different mechanism was inferred. In this system, Wang and Qin[85] established the presence of metallic nickel upon charge and discharge cycles using XPS and x-ray diffraction. From these results and the previous findings of Tarascon et al[89]. and Dahn et al.[90] they have suggested the following charge/discharge reaction mechanism involving the reversible formation of metallic Ni and lithium oxide:

$$\underset{\text{(charge)}}{NiO + 2Li^+ + 2e^-} \leftrightarrow \underset{\text{(discharge)}}{Ni + Li_2O} \qquad (5.5)$$

The presence of Ni from x-ray diffraction measurements indicates that in Li based electrochromic devices bulk ion transport may be important. Whether or not electrochromic reactions take place at the surface or within the bulk, the relative density remains an important film property for the nickel oxide ion storage layer.

Highly oriented crystalline NiO films (111) have been obtained by Fujii et al.[81] through PECVD using nickel acetylacetonate ($Ni(acac)_2H_2O$ acac= $C_5H_7O_2$) and O_2. Deposition was carried out in a symmetric capacitively-coupled plasma chamber. Substrate temperature and chamber pressure were fixed at 400 °C and 1000 mTorr, respectively. The $Ni(acac)_2$ source was heated to 166°C in a vaporizer and delivered to the chamber by nitrogen carrier gas through heated gas lines at flow rate of 50 cm^3/min. Oxygen flowrate was varied from 3 to 150 cm^3/min. With O_2 flow rate as the only process variable, the authors found that the highest growth rate was achieved at the lowest O_2 flow rate which produced highly oriented NiO (111) films. Increasing the O_2 flow rate shifted the NiO orientation to (100) and the growth rate decreased.

The work by Fujii et al.[81] proves that PECVD of NiO is possible, however the authors explored only a limited processing parameter space. Furthermore, no subsequent characterizing the PECVD grown NiO with respect to battery or electrochromic applications was discussed. $Ni(acac)_2$ has been shown to be a viable precursor, however nickel carbonyl ($Ni(CO)_4$) possesses more favorable properties as a nickel source with respect to its vapor pressure. $Ni(CO)_4$ is a liquid at room temperature with a vapor pressure of 400 Torr at 26°C and a boiling point of 43°C. Use of this precursor would

likely allow the nickel to be introduced to the chamber through gas lines at or close to room temperature. It is also likely that the crystalline films obtained by Fujii et al. are a strong function of the elevated substrate temperature of 400°C. Lowered substrate temperatures are desirable and it may be possible to also deposit NiO at or close to room temperature using PECVD. Lowered substrate temperatures may also produce amorphous films of NiO. Analogous to tungsten oxide film, amorphous films of NiO may also show better electrochromic properties than highly oriented films. The overall favorable optical properties of solid-state devices incorporating NiO in electrochromic devices merits future PECVD study of processing conditions and resulting electrochromic performance of PECVD NiO films.

5.2 The Electrolyte

5.2.1 Requirements and Characterization

The role of the electrolyte is to conduct the light ions between storage and electrochromic layers. To transport ions between storage and electrochromic this film must processes a high ionic conductivity, while maintaining low electric conductivity. Electron transport leads to gradual self-bleaching, and does not allow the device to display open-circuit memory. Maintaining an open-circuit memory would also allow devices to reach any intermediate coloration level.

The requirement of the ion conductor to carry ionic current while remaining electrically insulating imposes a slightly different methodology in evaluating film

performance. Specifically, ion conductivity is measured with regard to ion mobility, μ, measured in cm^2/Vs. The resulting conductivity is given by

$$\sigma_{DC} = nq\mu \tag{5.6}$$

where q is the charge of the ionic species and n is the number density of ionic charge carriers. Response time of the electrolyte is directly proportional to the ion's mobility and the applied electric field. The velocity, v, of the ions in an applied electric field, E, is given by

$$v = \mu E \tag{5.7}$$

Ion conductivity is typically determined from ac impedance techniques. However, isothermal transient ionic current (ITIC) measurements are necessary to separate the contributions of both ion density and ion mobility to the overall conductivity[91]. Similar to the PITT approach, this technique measures the current response in time to an applied voltage with other parameters held constant. From Faraday's law one finds the current response as a function of film thickness, L, surface area, S, applied potential, V_a time, t and mobility[91].

$$I(t) = \frac{S\sigma_{DC}V_a}{L}\exp(\frac{-\mu V_a}{L^2}t) \tag{5.8}$$

By fitting the parameters in the above equation to the transient current response the mobility can be determined. Using the initial current one can estimate the conductivity and back out the carrier concentration.

5.2.2 Ta_2O_5

Numerous complete electrochromic devices have been prepared using either liquid organic or solid state inorganic electrolytes[39,63]. While liquid electrolytes are convenient for fundamental studies of electrochromism, they are not in general agreed upon for practical applications since gravity induced forces may be excessive when large areas are of interest[39]. Also the long-term stability to sun exposure is a concern. Solid-state electrochromic devices have been prepared with electrolytes of $RbAg_4I_5$[92], $NaZrSiP_3O_{12}$[93], LiF[94], $LiAlF_3$, MgF_2[60], and Ta_2O_5[95,96]. However, most of these materials are typically only achievable through PVD techniques. Tantalum pentoxide remains the only suitable choice for this application that can be easily fabricated by PECVD.

As with all of the previously discussed films, Ta_2O_5 has been deposited through a variety of deposition techniques, including anodic oxidation[97], thermal oxidation of Ta[98], r.f sputtering[99], CVD[100], and PECVD[101-103]. Tantalum oxide thin films are of special interest in the semiconductor industry as a dielectric material for dynamic random access memory (DRAM) applications[104]. The extremely high dielectric constant and low leakage currents attainable in Ta_2O_5 are the driving forces for this development. There have been several studies on PECVD grown Ta_2O_5[101-103] focused on semiconductor applications.

The source of the tantalum in PECVD processes is typically $TaCl_5$ or $Ta(OC_2H_5)_5$. Oxygen or N_2O is combined with these precursors to deposit thin films of Ta_2O_5. Unlike films of WO_3 or V_2O_5 that have been grown at room temperature, PECVD of Ta_2O_5 still requires substrate temperatures[101,102] in the range of 200-600°C. To

minimize leakage currents, all studies found that high temperature annealing of up to 900°C was required for DRAM applications. However, the as deposited leakage current of 10^{-10} mA/cm^2 reported by S.R. Jeon et al.[103] at 400°C would most likely still be a suitable application as an electrolyte in an electrochromic application.

While the leakage current of reported PECVD grown Ta_2O_5 is suitable for electrochromic applications, there has been no characterization of ionic mobilities in PECVD Ta_2O_5. As with all thin films, properties are inherently linked to deposition technique. Mattsson and Niklasson[105] used ITIC to measure proton an Li^+ mobility in tantalum oxide films grown by traditional CVD and found Li^+ and H^+ mobilities of 1.2 x 10^{-11} and 3.0 x 10^{-10} cm^2/Vs, respectively. While pulsed laser deposition work carried out by Fu and Qin[106] found Li^+ mobilities also measured by ITIC techniques to be two order of magnitude less than the CVD films. The control of ion conductivity in WO_3 by PECVD demonstrated in this warrants a PECVD investigation of Ta_2O_5. Furthermore, devices in the literature incorporating Ta_2O_5 as the electrolyte are typically deposited only by r.f. sputtering[95,96], and no reports on PECVD Ta_2O_5 electrolytes could be found.

5.3 Recommendations for Electrolyte and Ion Storage Layers

Fabrication of a complete electrochromic device entirely by PECVD is desirable for a two main reasons. First, the inherent versatility of PECVD may be used to conveniently tailor the properties of the necessary films required for an electrochromic

device. The work presented in this thesis demonstrates how PECVD can be used to optimize the properties of WO_3 for application in electrochromic devices. Modulation of precursor gases could enable the entire device to be deposited in a single system. This one step process could minimize interfacial defects. Second, there are several aspects to PECVD that make it more economical than PVD. Typically, transport of source materials using PVD requires pressure regimes below 10^{-5} Torr. PECVD is typically carried out in pressures around 10^{-3} Torr, in this pressure range the chamber can be mechanically pumped, eliminating the need for more expensive high vacuum pumping systems.

Tantalum pentoxide is the most viable choice as an electrolyte in a PECVD electrochromic device. However, the numerous examples in the literature of PECVD grown Ta_2O_5 focus exclusively on applications for DRAM memory. These reports all indicate that a substrate temperature of 400°C with post deposition annealing was required to achieve the extremely small leakage currents demanded by today's high-performance memory applications. However, these high temperatures would be detrimental to the properties of amorphous tungsten oxide. Tungsten oxide begins to transition from amorphous to polycrystalline at 300°C, and the polycrystalline structure is detrimental to the switching time in an electrochromic device. The key to development of PECVD grown Ta_2O_5 for electrochromic applications would be to find a minimum temperature that still produces a film with minimal electron leakage currents for an electrochromic device. In addition, the thickness would also need to be optimized with respect to electronic leakage and optical transmission.

Both nickel and vanadium oxides are suitable for application as storage layers in an electrochromic device. Typically, vanadium oxide is the film of choice for devices based on Li^+ intercalation, while NiO is used in proton based devices. In the production of smart windows, it is generally agreed upon that Li^+ based devices have increased cycle life and environmental stability over H^+ based devices. It is cycle lifetime that is the dominant deciding factor in the large scale production of smart windows. Therefore, the recommended storage layer in a PECVD device would be vanadium oxide despite its less than optimal optical properties. The key to development of V_2O_5 would be optimization of an adequate thickness and intercalation level with respect to its optical properties. Film density will also likely effect ion transport kinetics and need to be optimized.

5.4 Towards a Complete PECVD Device

The current electrochemical set-up presented in this thesis for analysis of WO_3 is not adequate for the evaluation of both electronic and ionic currents in prepared samples of Ta_2O_5. Because of this constraint, it is recommended that the next step to a PECVD device would be the fabrication of the V_2O_5 ion storage layer for the central reason that this layer could be characterized by the same techniques presented in this thesis. A complete device cannot be fabricated without an electrolyte, however a complete device could easily be finished through use of a solid organic electrolyte. While organic electrolytes are not in general desirable for large-scale production they can be used on an

experimental scale to examine complete device dynamics. The TCO and electrochromic WO_3 films deposited by PECVD could be joined by a solid organic lithium based electrolyte to the PECVD ion storage and TCO layers. Figure 5.1 shows a schematic of such a device. Parts A and B are fabricated separately by PECVD and joined by an organic electrolyte and epoxy resin.

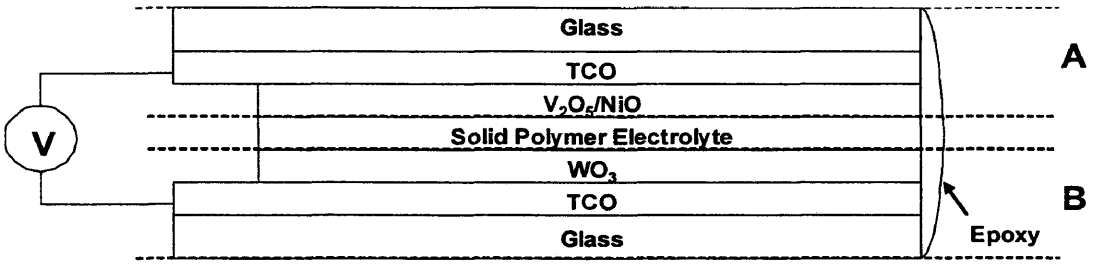

Figure 5.1: Schematic of solid state device using organic electrolyte.

A similar device was prepared by Zhang et al.[107] from thermally evaporated sources of WO_3 and V_2O_5. In their work they were able to construct 2" x 2" optimized devices that can switch between 74 and 12 percent transmittance at 633 nm in one minute under coloration and bleaching potentials of -1.8 V and 1.2 V, respectively. Their work outlines the experimental procedures for preparing the organic electrolyte from PMMA, ethyl acetate, and lithium perchlorate. A device recipe for both the preparation of the polymer and film thicknesses is presented that maximized device transmission modulation. Under these guidelines, similar PECVD devices could be constructed and directly compared to the thermally prepared devices. The direct comparisons between

PECVD films and PVD films will provide valuable insight into the viability of PECVD as the best choice for large-scale production of electrochromic devices.

REFRENCES CITED

[1] S. K. Deb, Philos.Mag. **22,** 801 (1973).

[2] O. F. Schrimer, J. Phys. (Paris) **6,** 479 (1980).

[3] J.-G. Zhang, C. E. Tracy, D. K. Benson, S. K. Deb, A.W.Czanderna, and C.Bechinger, J. Electrochem. Soc. **144,** 2022-2025 (1997).

[4] C. G. Granqvist, A. Azens, J. Isidorsson, M. Kkarrazi, L. Kullman, T. Lindstrom, G. A. Niklasson, C. G. Ribbing, D. Ronnow, M. S. Mattsson, M. Veszelei, J. Non-Cryst. Solids. **218,** 273 (1997).

[5] http:\\www.nrel.gov/buildings/windows/benfits.html.

[6] A. Gutarra, A. Azens, B. Stjerna, and C.G.Granqvist, Appl. Phys. Lett. **64,** 1604 (1994).

[7] A. Azens, L. Kullman, D. D. Ragan, C.G.Granqvist, and B. Hjorvasson, Appl. Phys. Lett. **68,** 3701 (1996).

[8] M. Veszelei, L. Kullman, A. Azens, C.G.Granqvist, and B. Hjorvarsson, J. Appl. Phys. **81,** 2024 (1997).

[9] K. Bange, Solar Energy Mater. Solar Cells **58,** 1-131 (1999).

[10] P. Tagstrom and U. Jansson, Thin Solid Films **352,** 107-113 (1999).

[11] R. G. Gordon, S. Barry, J. T. Barton, and R. N. R. Broomhall-Dillard, Thin Solid Films **352,** 107 (2001).

[12] K. D. Lee, Thin Solid Films **302** (1997).

[13] P. K. Shen, K. Y. Chen, and A. C. C. Tseung, J. Electrochem. Soc. **141,** 1758 (1994).

[14] M. A. Lieberman and A. J. Lichtenberg, *Principles of Plasma Discharges and Materials Processing, Chapter 11* (Wiley, New York, 1994).

[15] C. E. Tracy and D. K. Benson, J. Vac. Sci. Technol. A **4,** 2377-2383 (1986).

[16] G. J. Sacks and W. B. Henley, J. Electrochem. Soc. **144,** 1045-1049 (1997).

[17] J. J. Robbins, R. T. Alexander, M.Bai, Y. J. Huang, and C. A. Wolden, J. Vac. Sci. Technol. A **19,** 2762-2766 (2001).

[18] J. J. Robbins, R. T. Alexander, W. Xiao, T. L. Vincent, and C. A. Wolden, Thin Solid Films **406,** 145 (2002).

[19] J. J. Robbins, J. Estaban, C. Fry, and C. A. Wolden, J. Electrochem. Soc. **150,** C693-C698 (2003).

[20] J. J. Robbins, M.S. Thesis, Colorado School of Mines, 2000.

[21] J. W. Coburn and M. Chen, J. Appl. Phys. **51,** 3134-3136 (1980).

[22] S. L. B. Cho, L. Sha, and J. P. Chang, J. Vac. Sci. Technol. A **19,** 27512761 (2001).

[23] R. T. A. J. J. Robbins, W. Xiao, T. L. Vincent and C. A. Wolden, Thin Solid Films **406,** 145-150 (2002).

[24] H. M. Katsch, A. Tewes, E. Quandt, A. Goehlich, T. Kawetzki, and H. F. Döbele, J. Appl. Phys. **88,** 6232-6238 (2000).

[25] J. Zhang, D. K. Benson, C. E. Tracy, and S. K. Deb, J. Mater. Res. **8,** 2657-2667 (1993).

[26] B. Vuillemin and O. Bohnke, Solid State Ionics **68,** 257 (1994).

[27] J. Wang, J. M. Bell, and I. L. Skryabin, Solar Energy Mater. Solar Cells **59,** 167-183 (1999).

[28] O. Bohnke, M. Rezrazi, B. Vullemin, C. Bohnke, and P. A. Gillet, Solar Energy Mater. Solar Cells **25,** 361 (1992).

[29] S. K. Mohapatra, J. Electrochem. Soc. **125,** 284 (1978).

[30] Z. Lou, Z. Ding, and Z. Jiang, J. Non-Cryst. Solids. **112,** 309 (1989).

[31] B. Reichman and A. J. Bard, J. Electrochem. Soc. **127,** 647 (1980).

[32] C. Ho, I. D. Raistrick, and R. A. Huggins, J. Electrochem. Soc. **127,** 343 (1980).

[33] J. Nagai and T. Kamimori, Jpn. J. Appl. Phys. **22,** 681-687 (1983).

[34] J. E. B. Randles, Discuss. Faraday Soc. **1,** 11 (1947).

[35] M. S. Mattsson, G. A. Niklasson, and C.G.Granqvist, J. Appl. Phys. **80,** 2169-2174 (1996).

[36] J. Crank, *The Mathematics of Diffusion* (Oxford University Press, London, 1967).

[37] J. McGraw, C. Bahn, P. Parilla, J. Perkins, D. Readey, and D. Ginley, Electrochimica Acta **45,** 187-196 (1999).

[38] J. D. Klein, A. Yen, and S. F. Cogan, J. Appl. Phys. **68,** 1825-1830 (1990).

[39] C.G.Granqvist, Solar Energy Mater. Solar Cells **60,** 201-262 (2000).

[40] C. Bittencourt, R. Landers, E. Llobet, G. Molas, X. Correig, M. A. P. Silva, J. E. Sueiras, and J. Calderer, J. Electrochem. Soc. **149,** H81-H86 (2002).

[41] C. Salinga, H. Weis, and M. Wuttig, Thin Solid Films **414,** 275 (2002).

[42] J. G. H. Mathew, S. P. Sapers, M. J. Cumbo, N. A. O'Brien, R. B. Sargent, V. P. Raksha, R. B. Lahaderne, and B. P. Hichwa, J. Non-Cryst. Solids. **218,** 342 (1997).

[43] C. G. Granqvist, *Handbook of Inorganic Electrochromic Materials* (Elsevier, Amsterdam, 1995).

[44] J. Zhang, C. E. Tracy, D. K. Benson, and S. K. Deb, J. Mater. Res. **8,** 2649-2656 (1993).

[45] K. Choi, W. Shin, and S. Yoon, J. Electrochem. Soc. **149,** F18 (2002).

[46] B. Cho, S. Lao, L. Sha, and J. P. Chang, J. Vac. Sci. Technol. A **19,** 27512761 (2001).

[47] B. C. Lai and J. Y. Lee, J. Electrochem. Soc. **146,** 266 (1999).

[48] D. Green, Applied Optics **29,** 4547-4549 (1990).

[49] A. Monteiro, M. F. Costa, B. Almeida, V. Teixeira, J. Gago, and E. Roman, Vacuum **64,** 287 (2002).

[50] L. S. Wang, B. P. Hichwa, S. P. Sapers, J.G.H.Mathew, and N. A. O. Brien; *Vol. The Electrochemical Society* (Pennington, 1995), p. 63-75.

[51] M. Seman and C. Wolden, J. Vac. Sci. Technol. A **21,** 1927-1933 (2003).

[52] B. Reichman and A. J. Bard, J. Electrochem. Soc. **126,** 583 (1979).

[53] M.A.Habib and D.Glueck, Solar Energy Mater. Solar Cells **18,** 127 (1989).

[54] C. J. Wen, B. A. Boukamp, R. A. Huggins, and W. Weppner, J. Electrochem. Soc. **126,** 2258 (1979).

[55] J. Gou, Y. J. Li, and M. S. Whittingham, J. Power Sources **54,** 461 (1995).

[56] J.Bludska and I. Jakubec, Z. Phys. Chem **194,** 69 (1996).

[57] *Handbook of Chemistry and Physics, 67th ed. p. B-141* (CRC Press, Boca Raton, FL, 1986-1987).

[58] N. Yoskiike and M. Ayusawa, J. Electrochem. Soc. **131,** 2600 (1984).

[59] R. S. Crandall, P. J. Wojtowicz, and B. W. Faughnan, Solid State Commun. **18,** 1409 (1976).

[60] C. Bechinger, J. N. Bullock, J.-G. Zhang, C. E. Tracy, D. K. Benson, and S. K. Deb, J. Appl. Phys. **80,** 1226-1232 (1996).

[61] R. D. Rauh and S. F. Cogan, J. Electrochem. Soc. **140,** 378 (1993).

[62] J. J. Robbins, Ph.D. Thesis, Colorado School of Mines, 2003.

[63] C.G.Granqvist, E. Avendano, and A. Azens, Thin Solid Films **442,** 201-211 (2003).

[64] Y. J. Park, K. S. Ryu, N.-G. Park, Y.-S. Hong, and S. H. Chang, J. Electrochem. Soc. **149,** A597-A602 (2002).

[65] M. Benmoussa, A. Outzourhit, A. Bennouna, and E. L. Ameziane, Thin Solid Films **405,** 11-16 (2002).

[66] M. Green and K. Pita, J. Appl. Phys. **81,** 3592-3600 (1997).

[67] N. Ozer, S. Sabuncu, and J. Cronin, Thin Solid Films **338,** 201-206 (1999).

[68] J.-G. Zhang, P. Liu, J. A. Turner, C. E. Tracy, and D. K. Benson, J. Electrochem. Soc. **145,** 1889-1892 (1998).

[69] D. Barreca, L. Armelao, F. Caccavale, V. D. Noto, A.Gregori, G. A. Rizzi, and E. Tondello, Chem. Mater. **12,** 98-103 (2000).

[70] A.Talledo and C.G.Granqvist, J. Appl. Phys. **77,** 4655-4666 (1995).

[71] S. F. Cogan, N. M. Nguyen, S. J. Perrotti, and R. D. Rauh, J. Appl. Phys. **66,** 1333-1337 (1989).

[72] A. Daneo, G. Macrelli, P. Polato, and E. Poli, Solar Energy Mater. Solar Cells **56,** 237 (1999).

[73] R. Lechner and L. K. Thomas, Solar Energy Mater. Solar Cells **54,** 139 (1998).

[74] D. S. Lee, D. D. Lee, H. R. Hwang, and J. H. Paik, J. Mater. Sci. Mater. Electr **12,** 41 (2001).

[75] D. W. Murphy and P. A. Christian, Science, 651 (1979).

[76] C. R. Otterman, A. Temmink, and K. Bange, Thin Solid Films **193/194,** 409 (1990).

[77] I. C. Faria, M. Kleinke, A. Gorenstein, M. C. A. Fantini, and M. H. Tabaciks, J. Electrochem. Soc. **145,** 235-240 (1998).

[78] J. S. E. M. Svensson and C.G.Granqvist, Appl. Phys. Lett. **49,** 1566 (1986).

[79] M. K. Carpenter, R. S. Connel, and D. A. Corrigan, Solar Energy Mater. Solar Cells **16,** 333 (1987).

[80] J. L. Garcia-Miquel, Q. Zhang, S. J. Allen, A. Rougier, A. Blyr, H. O. Davies, A. C. Jones, T. J. Leedham, P. A. Williams, and S. A. Impey, Thin Solid Films **424,** 165-170 (2003).

[81] E. Fujii, A. Tomozawa, H. Torii, and R. Takayama, Jpn. J. Appl. Phys. Part 2, Lett. **35,** L328-L330 (1996).

[82] D. A. Corrigan, Solar Energy Mater. Solar Cells **25,** 293 (1992).

[83] K.-S. Ahn, Y.-C. Nah, and Y.-E. Sung, J. Appl. Phys. **92,** 1268-1273 (2002).

[84] D. A. Wruck and M. Rubin, J. Electrochem. Soc. **140,** 1097-1104 (1993).

[85] Y. Wang and Q.-Z. Qin, J. Electrochem. Soc. **149,** A873-A878 (2002).

[86] K.-W. Nam and K.-B. Kim, J. Electrochem. Soc. **149,** A346-A354 (2002).

[87] J. Nagai, G. D. McMeeking, and Y. Saitoh, Solar Energy Mater. Solar Cells **56,** 309 (1999).

[88] A.Azens, L. Kullman, G.Vaivars, H.Nordborg, and C.G.Granqvist, Solid State Ionics **113-115,** 449 (1998).

[89] P.Poizot, S.Laruelle, S.Grugeon, L.Dupont, and J.-M. Tarascon, Nature (London) **407,** 496 (2000).

[90] M. N. Obrovac, R. A. Dunlap, R. J. Sanderson, and J. R. Dahn, J.E **148,** A576 (2001).

[91] M. Watanabe, M. Rikukawa, K. Sanai, and N. Ogata, J. Appl. Phys. **58,** 736 (1985).

[92] M. Green and D. Richman, Thin Solid Films **24,** S45 (1974).

[93] G. G. Barna, J. Electron. Mater. **8,** 153 (1979).

[94] H. J. Stocker, S. Singh, L. G. VanUitert, and G. J. Zydzik, J. Appl. Phys. **50,** 2993 (1979).

[95] M. Kitao, H. Akram, K. Urabe, and S. Yamada, J. Eletronic. Mater, **21,** 419-422 (1992).

[96] E. B. Franke, C. L. Trimble, J. S. Hale, M.Scubert, and J. A. Woollam, J. Appl. Phys. **88,** 5777-5784 (2000).

[97] H. Sunami, T. Kure, N. Hashimoto, K. Itoh, and S. Asai, IEEE Electron Device Lett. **EDL-4,** 90 (1983).

[98] M. A. Mohammed, Thin Solid Films **176,** 45 (1989).

[99] S. Seki, T. Unagami, O. Kogure, and B. Tsujiyama, J. Vac. Sci. Technol. A **5,** 1771 (1987).

[100] M. Matsui, S. Oka, K. Yamagishi, K. Kuroiwa, and Y. Taruiet, Jpn. J. Appl. Phys. **27,** 506 (1988).

[101] F.-C. Chiu, J.-J. Wang, J. Y.-m. Lee, and S. C. Wu, J. Appl. Phys. **81,** 6911-6915 (1997).

[102] D. Laviale, J. C. Oberlin, and R. A. B. Devine, Appl. Phys. Lett. **65,** 2021-2023 (1994).

[103] S. R. Jeon, S.W.Han, and J. W. Park, J. Appl. Phys. **77,** 5978-5981 (1995).

[104] C. Hashimoto, H. Oikawa, and N. Honma, IEEE Trans. Electron Devices **36,** 14 (1989).

[105] M. S. Mattsson and G. A. Niklasson, J. Appl. Phys. **85,** 8199-8204 (1999).

[106] Z.-W. Fu and Q.-Z. Qin, J. Electrochem. Soc. **147,** 4610-4614 (2000).

[107] J.-G. Zhang, D. K. Benson, C. E. Tracy, S. K. Deb, A. W. Czanderna, and R. S. Crandall, J. Electrochem. Soc. **141,** 2795-2800 (1994).